UNIVERSITÀ DEGLI STUDI DI MODENA E REGGIO EMILIA

Dipartimento di Scienze Fisiche, Informatiche e Matematiche

Master's Degree in Physics

Monte Carlo Model Tuning for an Independent Dose Calculation Software: Testing and Validation of Optimal Parameters in Clinical Radiotherapy Treatment Plans

Supervisor:
Prof. Gabriele Guidi

Co-supervisor:
Dr. Valeria Trojani

Candidate:
Ayman El Ouati

ACADEMIC YEAR 2024/2025

Acknowledgments

I would like to sincerely thank Dr. Mauro Iori, Head of the Medical Physics Unit at AUSL-IRCCS of Reggio Emilia, for giving me the opportunity to carry out this thesis within the Department. It has been a real privilege to be part of such a dynamic and inspiring environment.

My gratitude also goes to my supervisor, Dr. Gabriele Guidi, for always being available and providing thoughtful feedback. His input truly helped me shape and improve my ideas throughout this project.

I am deeply thankful to Dr. Valeria Trojani, whose support has been a constant presence during every step of this thesis. Her help and availability have been essential, and her presence, even in the most challenging moments, has been a true source of strength throughout the time we shared.

I would like to express my heartfelt thanks to Dr. Elisabetta Cagni for allowing me to take part to this project. Her insight and innovative perspective taught me a great deal about how to approach a scientific project with depth and purpose, something I will certainly carry with me.

I am also especially thankful to Dr. Laura Verzellesi for her constant encouragement and genuine support, always offered with a cheerful, kind, and friendly attitude.

And finally, I am truly grateful to the entire Medical Physics Unit. From the beginning, you made me feel welcome as a member of your big family. Working with all of you has been one of the most rewarding parts of this experience.

Abstract

The present thesis work was carried out at the AUSL-IRCCS Medical Physics Unit, Reggio Emilia, Italy, and focuses on activities related to **Patient-Specific Quality Assurance** (**PSQA**), particularly on dosimetric verification through independent dose calculation in radiotherapy. The dosimetric check plays a crucial role in this process by comparing the dose calculated by the **Treatment Planning System** (**TPS**) with that recalculated independently by software such as RadCalc, in order to detect clinically relevant discrepancies.

The purpose of this study was to validate the **RadCalc's Monte Carlo calculation module** (**RCMC**), with a specific focus on the **Additional Radiation to Light Field Offset** (**ARLFO**) parameter, which characterizes the **multileaf collimator** (**MLC**) dosimetric parameter in the clinical planning and corresponds to the **Dosimetric Leaf Gap parameter** (**DLG**) used in TPS. The optimal ARLFO value was derived through an analytical method, starting from the standard baseline of 0 cm, in order to maximize the agreement with phantom-based PSQA measurements. The percentage dose difference between the point dose measured at the **central axis position** (**CAX**) inside the dedicated water phantom and that calculated by RCMC was evaluated for several fields with varying MLC apertures, ranging from 2 mm to 20 mm. The procedure has been conducted for 6 MV (6X) beams energy and results demonstrated a linear dependence between the dose difference at the CXS and the ARLFO value for each field. From this linear relationship, the ARLFO value that theoretically yields a 0% dose difference was extrapolated and considered optimal. Since the sensitivity to ARLFO increases as the field size decreases, a weighted average of the optimal ARLFO value for each field was calculated, with weights based on the MLC field aperture. The resulting weighted value was **−0.053 cm** for 6X energy.

Subsequently, a dataset of **26 clinical treatment plans** was analyzed, involving different tumor sites (breast, lung, head and neck, brain). For each plan, measurements and RCMC dose calculations were compared using both standard ARLFO = 0.000 cm and the optimal ARLFO = -0.053 cm configurations. Agreement was assessed using the **gamma index analysis**, applying both the 3%/2 mm criterion,

with a 10% global dose threshold and 3%/3 mm with a 50% local dose threshold. The gamma index evaluates the level of agreement between two dose distributions by combining spatial and dosimetric tolerances. Results showed an average improvement of 6 percentage points in gamma passing rates when using the optimal ARLFO value, confirming the field-size sensitivity of the parameter.

The analytical method developed in this study to determine the optimal ARLFO value was proved to be both feasible and straightforward to apply. It led to a noticeable improvement in the agreement between the measured dose and that based on RCMC calculation. In the near future, this approach can be extended to other beam energies, with the specific aim to identify the most appropriate parameter values to integrate into routine clinical practice.

Contents

1 Introduction: Fundamentals of Radiotherapy **1**
- 1.1 Interaction of Radiation with Matter . . . 2
- 1.2 Clinical linear accelerators . . . 4
- 1.3 Advanced radiotherapy techniques: IMRT and VMAT . . . 5
  - 1.3.1 Intensity-Modulated Radiation Therapy (IMRT) . . . 6
  - 1.3.2 Volumetric Modulated Arc Therapy (VMAT) . . . 7
- 1.4 Treatment Planning Systems in Modern Radiotherapy . . . 8
  - 1.4.1 Dosimetric Modeling and Dose Calculation Algorithms . . . 8
- 1.5 Radiation therapy workflow . . . 9

2 IDC Methods for Patient-Specific Quality Assurance **13**
- 2.1 Patient-Specific Quality Assurance . . . 13
- 2.2 Dosimetric Uncertainties in Small Fields . . . 15
- 2.3 Independent Dose Calculation in PSQA . . . 16
- 2.4 Dose Calculation Algorithms . . . 17

3 Materials and Methods **21**
- 3.1 Aim of the Study . . . 21
- 3.2 Software . . . 22
  - 3.2.1 Treatment Planning System (TPS) . . . 22
  - 3.2.2 RadCalc 3D Monte Carlo . . . 23
  - 3.2.3 Introduction to Verisoft software . . . 23
- 3.3 OCTAVIUS 4D . . . 25
- 3.4 Gamma Index Analysis . . . 26
- 3.5 Verification of the RCMC performance . . . 26
- 3.6 Methodology for ARLFO optimization in RCMC dose verification . . . 28
- 3.7 Validation of the Optimal ARLFO Parameter . . . 31
- 3.8 Extraction of MLC relevant parameters from Clinical Plans . . . 32
- 3.9 Statistical Analysis . . . 33

4 Results and Discussion **35**
4.1 Preliminary validation of RCMC against TPS: Analysis on open square fields 35
4.2 Tuning of ARLFO parameter 37
4.3 Comparison between measured dose and RCMC calculation 45
4.4 Statistical Anlysis 45
4.5 Investigation of anatomical site influence 46
4.6 Perspectives for Future Investigations 46

5 Conclusions **51**

A Matlab Script **53**

References **57**

Chapter 1

Introduction: Fundamentals of Radiotherapy

Radiation therapy is a medical discipline that uses **ionizing radiation** to destroy or irreversibly damage tumor cells, thus preventing their proliferation. The therapeutic mechanism is based on the interaction of radiation with cellular DNA, either directly or indirectly via free radical formation. The most lethal damage, such as double-strand breaks of the DNA, can inhibit cell division and lead to cell death [1]. Cancer is one of the major causes of death worldwide, and its incidence is steadily increasing, particularly in developing countries. According to the World Health Organization, approximately 50% of cancer patients undergo radiation therapy during the course of their treatment, and it contributes to the definitive cure in about 40% of cases [2].

Over time, radiation therapy has evolved considerably, transitioning from **two-dimensional** (**2D**) **techniques** based on simple radiographic images to modern **Three-Dimensional Conformal Techniques** (**3DCRT**), **Intensity-Modulated Radiation Therapy** (**IMRT**), **Image-Guided Radiation Therapy** (**IGRT**) and **Stereotactic Body Radiation Therapy** (**SBRT**). These techniques allow high-dose delivery to the tumor site while preserving surrounding healthy tissues [3]. Depending on clinical requirements, radiation beams can be generated using photons, electrons, protons, or even heavier ions.

From a clinical perspective, radiotherapy may be employed with a curative intention (e.g., in testicular, prostate, cervical, rectal, head and neck cancers) or with palliative purposes, to alleviate symptoms in advanced disease stages. It may be used alone or in combination with surgery, chemotherapy, or immunotherapy [1]. Each treatment is personalized based on patient anatomy, tumor characteristics, and biological considerations such as tissue radiosensitivity and fractionation schemes.

In this context, radiation therapy remains not only a cornerstone in modern oncology but also a field characterized by rapid technological and medical progress,

aiming to deliver more effective and less toxic treatments.

1.1 Interaction of Radiation with Matter

Understanding the interaction between ionizing radiation and matter is fundamental to the clinical application of radiation therapy. These interactions determine how radiation energy is deposited in biological tissues, influencing both treatment effectiveness and the risk to surrounding healthy structures.

Photon attenuation in matter follows an exponential decay in intensity, governed by the tissue-specific linear attenuation coefficient μ. This principle is fundamental in radiotherapy, as it enables the precise modulation and shaping of the radiation beam to optimize tumor dose delivery while minimizing exposure to surrounding healthy tissues [4]. The principal interactions relevant to therapeutic photon beams are the photoelectric effect, Compton scattering, and pair production. In Figure 1.1 the probability of the main photon interaction mechanisms is plotted as a function of photon energy and atomic number Z.

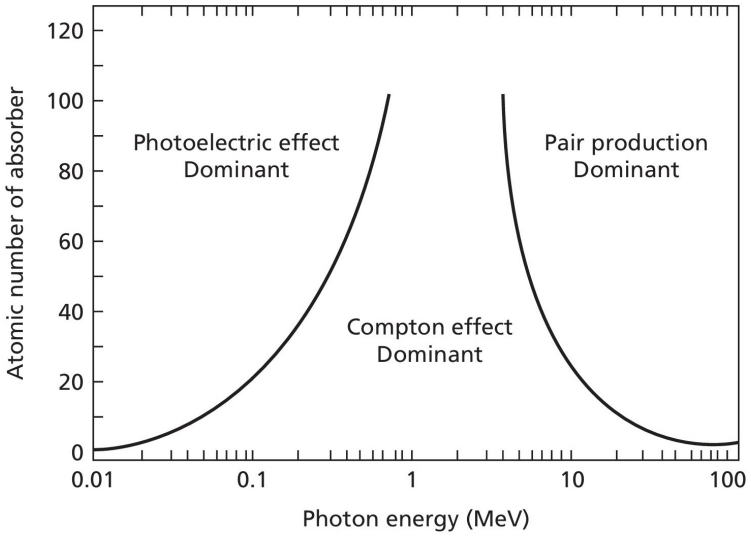

Figure 1.1: Dominant photon interaction mechanisms as a function of photon energy and atomic number. The photoelectric effect dominates at low energies and high atomic numbers, Compton scattering is dominant at intermediate energies, and pair production becomes significant at high energies and high-Z materials. Adapted from Pawlicki et al. [4].

The Photoelectric Effect

The **photoelectric effect** occurs when an incident photon transfers all its energy to a tightly bound inner-shell electron, which is subsequently ejected from the atom.

The energy of the ejected electron is equal to the difference between the incident photon energy and the binding energy of the electron. This effect is predominant at lower photon energies (typically below 100 keV) and is strongly dependent on the atomic number Z of the material, varying approximately as Z^3 [4]. Consequently, it plays a critical role in diagnostic imaging and in tissues or media with high atomic number components, such as bone or contrast agents.

In radiotherapy, although the photoelectric effect is less dominant at megavoltage energies used for deep-seated tumors, it remains relevant in dose deposition near interfaces with high-Z materials [3].

Compton Scattering

Compton scattering is the dominant interaction mechanism in soft tissues for photon energies ranging from about **100 keV to 10 MeV**, which includes the energy spectrum commonly used in external beam radiotherapy. In this process, an incident photon interacts with a loosely bound outer-shell electron, transferring part of its energy to the electron and scattering at a different angle with reduced energy [5].

The probability of Compton interaction is relatively independent of the atomic number and is primarily proportional to the electronic density of the material. Thus, Compton scattering particularly is suitable for describing homogeneous dose distributions in tissues of similar density, such as muscle, fat, and organs [3].

Pair Production

At photon energies above 1.022 MeV, **pair production** may occure. In this process, a photon interacts with the electromagnetic field of a nucleus and transforms into an electron-positron pair. The exceeding energy beyond the threshold is shared as kinetic energy between the two particles. Pair production probability increases with both photon energy and atomic number Z of the absorbing material [5].

While pair production is negligible at diagnostic imaging energies, it becomes progressively significant in high-energy photon beams (typically $> 10MeV$), especially in high-Z shielding materials or within linear accelerators' targets. Its clinical relevance grows in modalities involving high-energy photon beams or in proton and heavy-ion therapy, where secondary radiation effects must be considered [3].

The energy-dependent prevalence of these three interaction types influences the choice of radiation beam energies and delivery techniques in radiotherapy. Low-energy beams (e.g., X-rays) result in higher surface dose due to increased photoelectric effect, whereas megavoltage beams achieve greater tissue penetration with

more uniform energy deposition through Compton interactions. Modern treatment planning must account for all relevant interaction types to optimize dose conformity [6].

Therefore, understanding these physical mechanisms is essential for interpreting dosimetric uncertainties, managing tissue heterogeneities, and ensuring accurate quality assurance in radiotherapy practice.

1.2 Clinical linear accelerators

Clinical linear accelerators (**LINACs**) represent the main radiation source for modern external beam radiotherapy. Their design is the result of decades of technological innovation, combining principles of electromagnetism, high-frequency electronics, and precision mechanics to deliver therapeutic beams with sub-millimetric accuracy. Figure 1.2 depicts the schematic view of the LINAC.

At the core of the accelerator is a linear accelerating waveguide, composed of an evacuated metallic structure where electrons are accelerated to megavoltage energies (typically 4–25 MeV) by microwave radiofrequency fields, with frequencies ranging between $10^3\,MHz$ and $10^4\,MHz$ [4].

In linear accelerators, electrons - injected from a thermionic electron gun - are steered through the waveguide and, upon reaching the desired energy, are directed via a bending magnet toward the treatment head. In **photon mode**, they strike a high-Z tungsten target, producing bremsstrahlung X-rays. These photons are then shaped by a primary collimator, optionally filtered by a **flattening filter** (**FFF**), and further modulated by a secondary collimator and a **multileaf collimator** (**MLC**). In **electron mode**, the target is removed, and the electron beam is widened using scattering foils, shaped by applicators [3].

The treatment head, housed within a rotating gantry, includes all beam-modifying and monitoring systems. The gantry enables 360° rotation around the patient, delivering beams from any angle. The point around which the gantry, collimator, and couch rotate defines the **mechanical isocenter**, which serves as the spatial reference for all treatments.

Central to beam shaping is the aforementioned MLC, which consists of multiple individually motorized tungsten leaves. These allow dynamic and patient-specific beam modulation, enabling advanced techniques such as IMRT and VMAT.

Before reaching the patient, the beam is analyzed by monitor ionization chambers, which measure output, symmetry, and flatness in real time. Any deviation from calibrated parameters leads to immediate interruption, ensuring patient safety [4].

This intricate integration of mechanical systems, electronic feedback, and radiation physics has made the LINAC a highly reliable and adaptable platform, capable

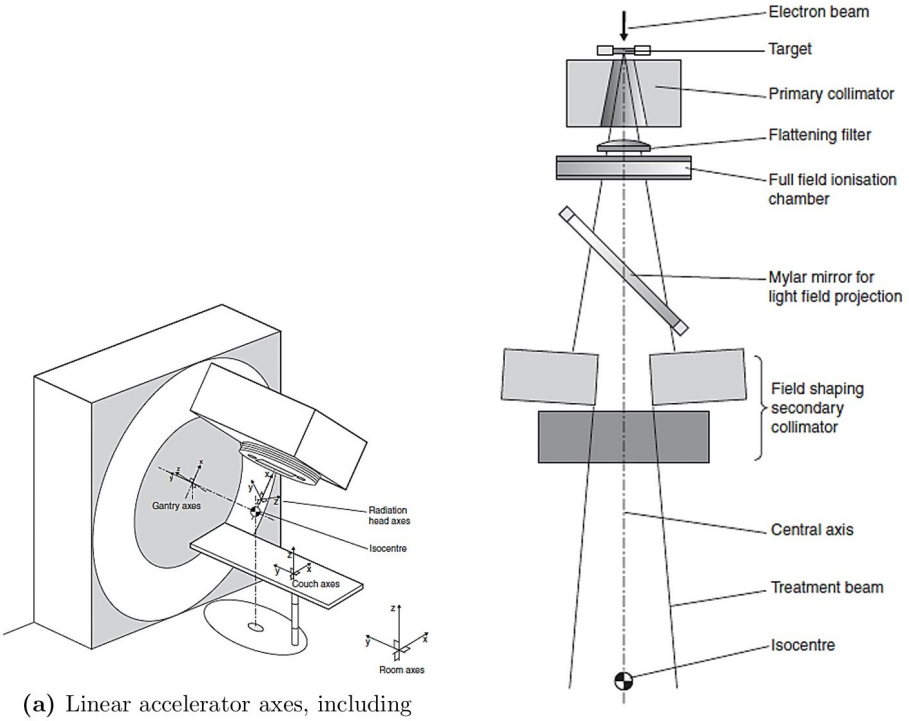

(a) Linear accelerator axes, including gantry, collimator, and couch.

(b) Detailed view of the LINAC head.

Figure 1.2: (a) Coordinate axes of a linear accelerator system, illustrating the mechanical degrees of freedom of the gantry, collimator, and treatment couch relative to the room and isocenter coordinates. (b) Schematic representation of the LINAC head, showing the electron beam path and key components including the target, primary collimator, flattening filter, ionization chamber, light field mirror, and multileaf secondary collimators. The central axis and treatment beam converge at the isocenter, enabling precise beam targeting. Adapted from Symonds et al. [6].

of delivering complex treatment plans with remarkable precision. Its versatility and clinical efficiency continue to evolve with the integration of imaging systems, adaptive planning algorithms, and motion management technologies.

1.3 Advanced radiotherapy techniques: IMRT and VMAT

The advent of modern radiotherapy has been marked by the development of increasingly conformal and sophisticated techniques aimed at maximizing tumor dose delivery while minimizing irradiation of surrounding healthy tissue. Among these, **Intensity-Modulated Radiation Therapy** (**IMRT**) and **Volumetric Modulated Arc Therapy** (**VMAT**) have become standard in many clinical settings due

to their ability to deliver highly precise, modulated dose distributions tailored to complex anatomical structures.

In general, both IMRT and VMAT represent major advancements in external beam radiotherapy (EBRT), offering enhanced dose conformity, organ preservation, and treatment personalization. Their implementation has been facilitated by the integration of advanced imaging, robust treatment planning systems, and refined accelerator technology.

1.3.1 Intensity-Modulated Radiation Therapy (IMRT)

Intensity-Modulated Radiation Therapy (**IMRT**) is an evolution of three-dimensional conformal radiotherapy that allows for modulation of beam intensity across individual fields. This is achieved through the dynamic movement of multileaf collimators during beam delivery, producing a large number of narrow "beamlets" of varying intensity. Treatment plans are generated through an *inverse planning* process, in which the desired dose to the tumor and constraints for organs at risk (OARs) are specified, and a computer algorithm optimizes the beamlet weights accordingly [7]. Figure 1.3 shows the 3D view from TPS for an IMRT plan, illustrating the beam arrangements and the resulting dose distribution in the patient geometry.

Two main IMRT delivery techniques exist: the *step-and-shoot* method, where radiation is delivered only when MLCs are stationary at predefined positions, and the dynamic MLC method, where radiation is continuously delivered as MLCs move. Both techniques allow for dose escalation and steep dose gradients, improving conformity and reducing toxicity [8].

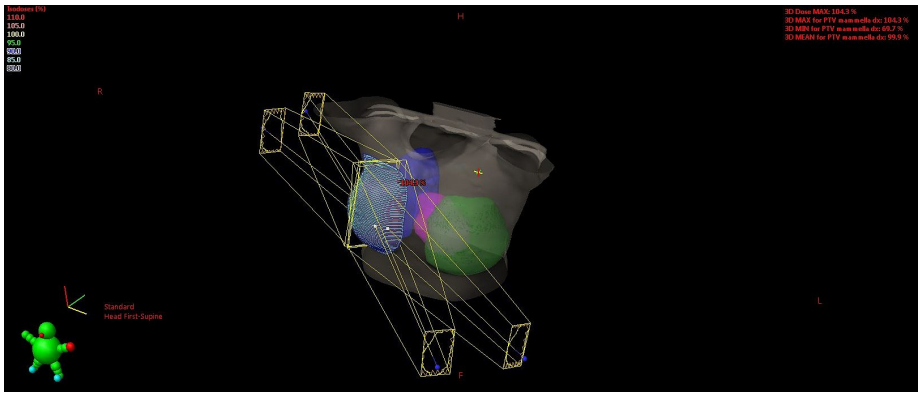

Figure 1.3: 3D view of an IMRT treatment plan in the Eclipse® TPS (Varian Medical Systems, Palo Alto, CA, USA), illustrating multiple fixed radiation fields and the corresponding dose distribution.

Clinically, IMRT has proven especially beneficial in treating head and neck cancers, prostate cancer, nervous system tumors, and gynecological malignancies, where

critical structures lie in close proximity to the tumor [6]. However, this technique is resource-intensive, requiring advanced planning software, increased quality assurance efforts, and longer treatment times due to higher monitor unit counts [8].

1.3.2 Volumetric Modulated Arc Therapy (VMAT)

VMAT builds upon the principles of IMRT by delivering modulated radiation dose while the linear accelerator's gantry rotates around the patient. During this arc-based delivery, three variables are dynamically adjusted: the MLC leaf positions, the dose rate, and the gantry speed [7]. This allows VMAT to achieve dosimetric outcomes comparable or superior to IMRT with significantly shorter treatment times and fewer monitor units. Figure 1.4 shows the 3D view for a VMAT plan, displaying the arc trajectory and corresponding dose distribution around the patient anatomy.

Introduced into clinical practice in the late 2000s, VMAT has demonstrated excellent efficacy in head and neck cancers, prostate cancer, brain tumors, and other complex sites. Comparative studies have shown that VMAT provides similar or improved target coverage and OAR sparing compared to IMRT, while reducing treatment delivery time by up to 50% and monitor units by over 30% [7]. This makes VMAT a preferred option in high-throughput clinical environments and in scenarios where patient comfort or motion management is critical.

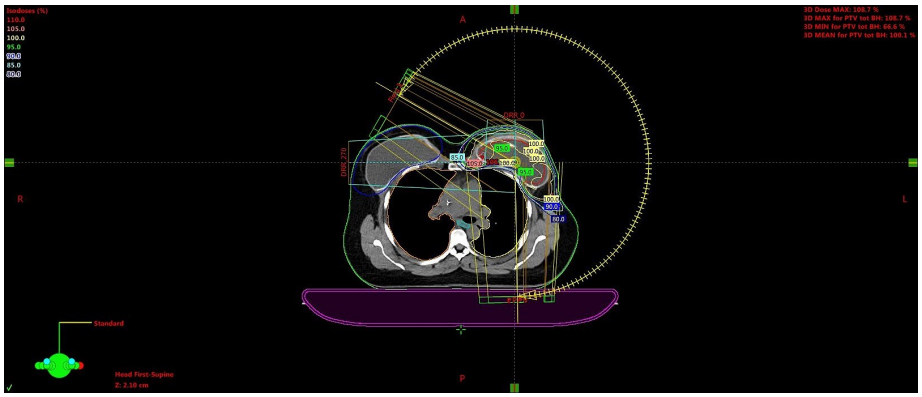

Figure 1.4: Axial view of a VMAT treatment plan in Eclipse® TPS (Varian Medical Systems, Palo Alto, CA, USA), showing dose distribution and continuous arc delivery around the patient.

1.4 Treatment Planning Systems in Modern Radiotherapy

The **Treatment Planning System** (**TPS**) serves as the computational and conceptual backbone of modern radiotherapy. It is a dedicated software environment where imaging data, anatomical segmentation, and machine-specific parameters are synthesized into an individualized treatment plan. The primary objective of a TPS is to simulate dose deposition in the patient's anatomy based on the selected beam geometry, modality, and energy, thereby enabling the achievement of therapeutic goals with high precision [3].

Historically, treatment planning was a largely manual process, involving geometric approximations and simple hand calculations. Nowadays, TPS platforms are highly automated and model-driven environments capable of supporting advanced techniques, including the aforementioned IMRT and VMAT. These systems incorporate complex physics models for dose computation, including pencil beam, convolution–superposition, and Monte Carlo algorithms, integrated within user-friendly graphical interfaces that conceal computational complexity while preserving accuracy.

A hallmark of modern TPS functionality is the use of inverse planning algorithms, which allow treatment planners to define clinical objectives - such as dose constraints for target volumes and OARs - while the software iteratively optimizes beam fluence, MLC configurations, and dose rates to meet those goals. This optimization process balances competing constraints and is often guided by objective functions weighted according to clinical priorities [7].

Beyond dose computation, the TPS provides an interactive visual environment for treatment design and verification. Key decision-support features include 3D dose visualization, isodose overlays on CT or MRI datasets, **Dose–Volume Histogram** (**DVH**) analysis, biological modeling tools, and feasibility metrics that assess plan quality. Many commercial systems now include modules for automated plan generation or plan scoring, improving workflow efficiency and promoting consistency across patients and operators.

The TPS also plays a central role in quality assurance, facilitating plan export in DICOM-RT format, support for phantom-based verification, and integration with record-and-verify systems.

1.4.1 Dosimetric Modeling and Dose Calculation Algorithms

At the core of every Treatment Planning System lies a set of physics-based models that govern dose calculation. These algorithms simulate how radiation interacts

with patient tissues, accounting for attenuation, scatter, and heterogeneity. According to established recommendations, the dose computation module must be validated through an extensive commissioning process that includes both model configuration and clinical qaulity assurence procedures.

Modern TPS platforms typically implement one or more of the following dose calculation strategies:

- **Pencil Beam Algorithms** – computationally fast but limited in accuracy for heterogeneous media and sharp dose gradients.
- **Convolution–Superposition Methods** – more accurate, particularly in soft tissue and near interfaces, as they model lateral electron transport and scattered radiation.
- **Monte Carlo Simulations** – regarded as the reference standard due to their stochastic modeling of particle interactions.

Clinical implementation of these algorithms requires machine-specific data such as PDD curves, beam profiles, output factors, and scatter conditions, all of which must be verified through independent measurements. Reports and task groups have emphasized the need for tolerance thresholds, dosimetric reproducibility, and system documentation to ensure reliability and traceability across different planning scenarios [3].

In clinical practice, parameters such as dose grid resolution, normalization schemes, and heterogeneity correction methods must be carefully selected by the planner to optimize both accuracy and computational feasibility.

An example of the commercial TPS of **Eclipse®** (Varian Medical Systems, Palo Alto, CA, USA), used at AUSL-IRCCS Reggio Emilia, is presented in Figure 1.5. The image displays a three-dimensional dose distribution overlaid on anatomical structures in multiple views, showcasing the system's advanced capabilities in dose visualization and treatment plan assessment.

1.5 Radiation therapy workflow

The **radiotherapy workflow** is a complex and multidisciplinary process that ensures the safe and effective delivery of ionizing radiation for therapeutic purposes. It is composed of a series of sequential and interdependent steps, each of which must be executed with precision and supported by robust clinical and physical validation procedures.

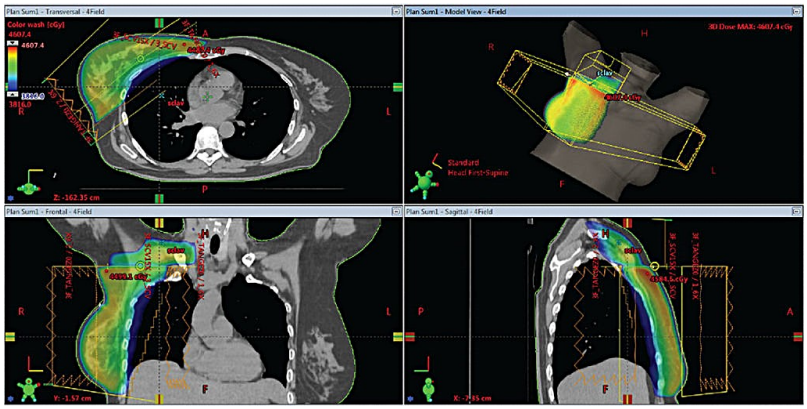

Figure 1.5: Interface of the Eclipse® TPS, showing a treatment plan with isodose color wash displayed across axial, coronal, sagittal, and 3D views.

The process begins with clinical consultation and patient referral, during which the radiation oncologist evaluates the indication for radiotherapy, defines therapeutic intent - curative or palliative - and considers integration with other treatment modalities. Once a treatment decision is made, the patient undergoes a simulation session, typically involving CT imaging in the treatment position. Immobilization devices are applied to ensure reproducibility across treatment fractions, and in many cases, multimodal imaging such as MRI or PET is acquired to improve the accuracy of tumor and OAR delineation [6].

The resulting image datasets are imported into the TPS, where they undergo registration and segmentation. At this stage, the radiation oncologist delineates the Gross Tumor Volume (GTV), Clinical Target Volume (CTV), Planning Target Volume (PTV), and relevant OARs (see Figure 1.6). These contours form the geometrical foundation of the treatment plan.

Treatment planning itself is typically conducted using inverse planning techniques. Clinical objectives - such as prescribed dose to the target and tolerance doses to nearby critical structures - are entered into the TPS, which uses optimization algorithms to generate beam configurations, fluence maps, and modulation schemes that satisfy these constraints. The resulting plan is evaluated with isodose distributions, 3D visualization tools, and DVHs [3].

A DVH is a plot that relates dose to volume, displaying for each dose level the fraction (or absolute amount) of a structure that receives it, thus condensing the 3D dose distribution into a two-dimensional graph. Examples of DVH curves are reported in Figure 1.7.

Two main variants are employed: the cumulative DVH (cDVH), which shows the percentage of volume receiving *at least* a given dose, and the differential DVH (dDVH), which shows the volume receiving dose within narrow bins. For example, in

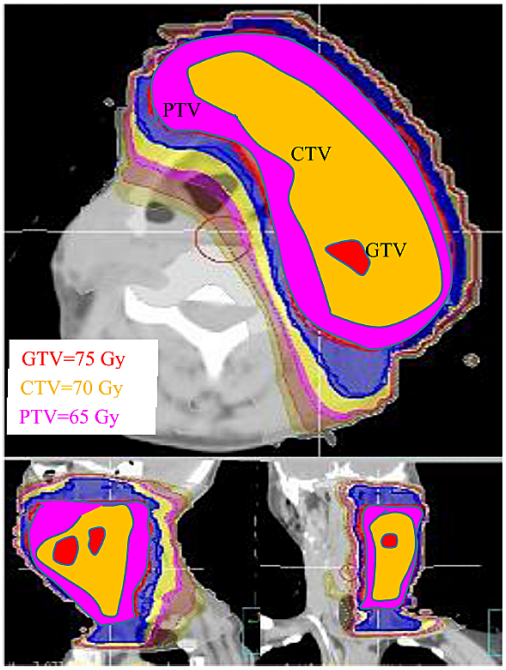

Figure 1.6: Example of structure contouring in radiotherapy planning. The image shows the delineation of the gross tumor volume (GTV), clinical target volume (CTV), and planning target volume (PTV), each associated with a prescribed dose level. Accurate contouring is a critical step in the radiotherapy workflow to ensure proper dose coverage and treatment effectiveness. Adapted from Dance et al. [3].

a cDVH a point at 95% on the dose axis and 98% on the volume axis indicates that 98% of the structure receives at least 95% of the prescribed dose. In OARs, ideal cDVH curves are steep and left-shifted, minimizing high-dose exposure; in targets, they should be right-shifted and plateau-shaped to ensure full coverage.

Despite their utility, DVHs lack spatial information and must be interpreted alongside direct inspection of the 3D dose distribution to detect potential under- or over-dosage in specific anatomical regions.

The process culminates in plan approval, typically involving peer review and physicist validation, followed by plan verification and quality assurance (QA) step. This step confirms that the dose calculated by the TPS is being accurately delivered to the patient, within clinically acceptable tolerances [3]. Pre-treatment QA typically includes phantom-based measurements, often using ionization chambers or Electronic Portal Imaging Devices (EPIDs), to validate the planned dose distribution and verify MLC dynamics. Minor discrepancies detected during this process may require plan adaptation to ensure that the dose to both the target and OARs remains within therapeutic limits [9].

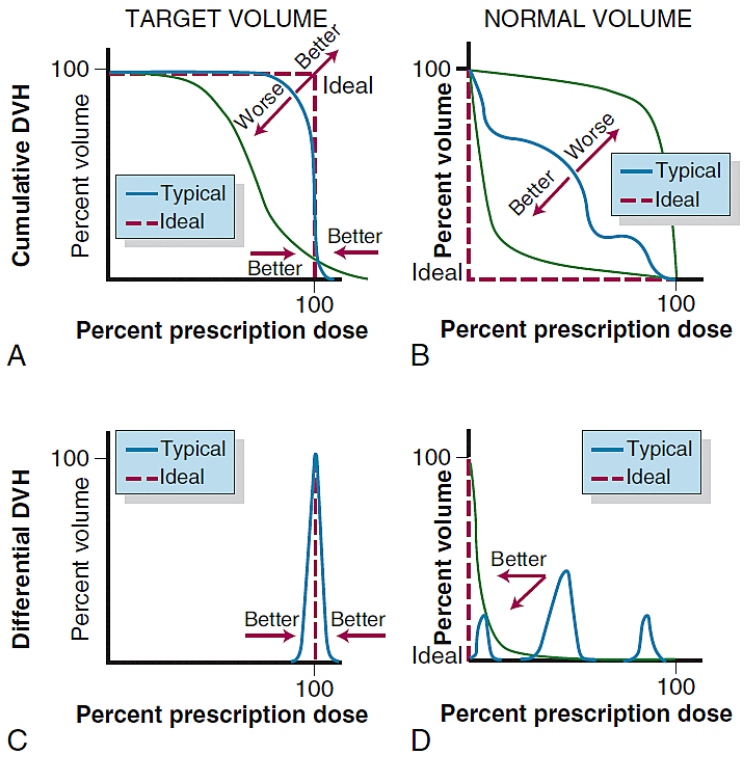

Figure 1.7: Ideal and typical dose–volume histogram (DVH) curves for target volumes (A, C) and normal tissues (B, D), presented as cumulative (A, B) and differential (C, D) distributions. These plots illustrate how an ideal plan delivers the full prescription dose uniformly to the target while minimizing exposure to surrounding healthy tissues. Better plan quality is associated with sharper target curves and steeper fall-off in normal tissue dose. Adapted from Symonds et al. [6].

As the treatment progresses, periodic assessments are conducted to monitor response and manage potential side effects. Adaptive strategies may be employed in cases of significant anatomical or biological change. Throughout the workflow, continuous optimization remains a priority to deliver a tumoricidal dose with maximum accuracy while preserving normal tissue function. Advances in imaging, computational power, and QA protocols collectively contribute to an increasingly personalized and precise radiotherapy process.

Chapter 2

IDC Methods for Patient-Specific Quality Assurance

2.1 Patient-Specific Quality Assurance

Patient-Specific Quality Assurance (**PSQA**) is a fundamental element in the safety and effectiveness of radiation delivery. It ensures that the planned dose distribution is faithfully delivered to the patient, maintaining therapeutic efficacy while minimizing risk to the surrounding healthy tissues. As advanced therapeutic techniques have introduced increasingly complex modulation schemes, the role of PSQA has become progressively more critical. Errors in dose calculation, plan transfer, or delivery can result in significant deviations from the intended treatment, compromising clinical outcomes [9] [10].

To address these risks, international organizations - such as the European Atomic Energy Community (EURATOM) and the American Association of Physisists in Medicine (AAPM) - have developed extensive guidance documents that describe a variety of tools and metrics — including 2D detector arrays, EPID-based verification, log-file analysis, and gamma index criteria — while emphasizing the necessity for institutional standardization and clear pass/fail thresholds.

Traditionally, PSQA has been performed through measurement-based verification. This involves delivering the approved treatment plan to a phantom and comparing the measured dose with the TPS-calculated distribution. Often, an independent secondary dose calculation is also performed, providing redundancy and increasing confidence in plan accuracy. In-vivo dosimetry and retrospective machine log analysis further complement the QA process, allowing for real-time and post-delivery checks. Despite its robustness, measurement-based verification PSQA is labor-intensive, time-consuming, and strictly dependent on physical measurement conditions.

In recent years an alternative approach has gained traction: Patient-Specific Quality Assurance based on **Independent Dose Calculation** (**IDC**). This methodology replaces - or complements - traditional measurements with a computational strategy, where the dose distribution is recalculated using an algorithm-based software that is independent from the TPS. This includes not only a separate dose engine (e.g., Monte Carlo) but also the use of distinct data workflows, such as different CT-to-density conversion tables and anatomical segmentation methods.

This IDC based PSQA process typically includes two stages:

- a recalculation of the dose using the original TPS plan;
- a recalculation based on a reconstructed plan derived from treatment delivery log files (log-plan), which captures the actual beam parameters as delivered during a treatment simulation.

Dose distributions from both recalculations are evaluated in patient geometry using 3D gamma analysis and comparison against clinical objectives, including DVH metrics.

One of the most compelling arguments in favor of this latter-explained process is its efficiency and scalability. Indeed, IDC requires significantly less beam time and can be automated within a digital workflow. This makes IDC a powerful tool for routine QA and opens the door to daily adaptive QA, enabling faster response to anatomical or technical variations over the treatment course.

Importantly, recent surveys — including those conducted in Canada, China, and by the *Imaging and Radiation Oncology Core* (IROC) center — have shown significant variability in PSQA implementation across institutions. Many centers still rely on resource-heavy approaches, and in some cases, QA practices remain inconsistent with TG-218 recommendations [9]. Initiatives such as the Ontario PCOP working group have demonstrated the value of collaborative efforts aimed at standardizing PSQA protocols and incorporating IDC into regular clinical workflows.

The integration of Independent Dose Calculation within the PSQA represents a natural and necessary evolution in radiotherapy quality assurance. By shifting from hardware-dependent verification to model-based recalculation, clinical teams can improve efficiency, reduce uncertainty, and ultimately provide more personalized and reliable treatments. Far from replacing measurment-based PSQA entirely, IDC serves as a complementary pillar one that aligns with the increasing demand for precision, adaptability, and accountability in radiation oncology.

2.2 Dosimetric Uncertainties in Small Fields

In clinical context a field is considered to be small when its dimensions are below $4\times4\,\mathrm{cm}^2$. In general, small fields represent unique challenges in radiotherapy dosimetry, which arise frequently in techniques such as IMRT and VMAT, where static fields or dynamic segments fall below conventional reference geometry. However, the dosimetric characterization of such fields is complicated by physical and geometric effects that invalidate the assumptions underlying standard dosimetry protocols [11].

Small fields are not strictly defined by size alone; rather, they are characterized by the occurrence of the following physical conditions [11]:

- the loss of lateral charged particle equilibrium (LCPE);
- partial occlusion of the photon source;
- detector volume effects.

Loss of Lateral Charged Particle Equilibrium (LCPE)

In small fields, the range of secondary electrons generated by photon interactions can exceed the field half-width. When this occurs, electrons escape the beam laterally before depositing their energy locally, leading to a dose underestimation in both field periphery and regions next to the detector [11].

Source Occlusion and Penumbra Broadening

The finite size of the primary photon source and the narrowing of the beam aperture cause partial occlusion of the radiation source by the collimators. This leads to an extended penumbra and reduced central beam uniformity, as schematically depicted in Figure 2.1. As the field size decreases, penumbrae may overlap, and the full width at half maximum (FWHM) of the dose profile can become broader than the nominal collimator setting. This is known as the *apparent field widening effect*. The magnitude of this discrepancy depends strongly on the source-to-collimator and source-to-detector distances.

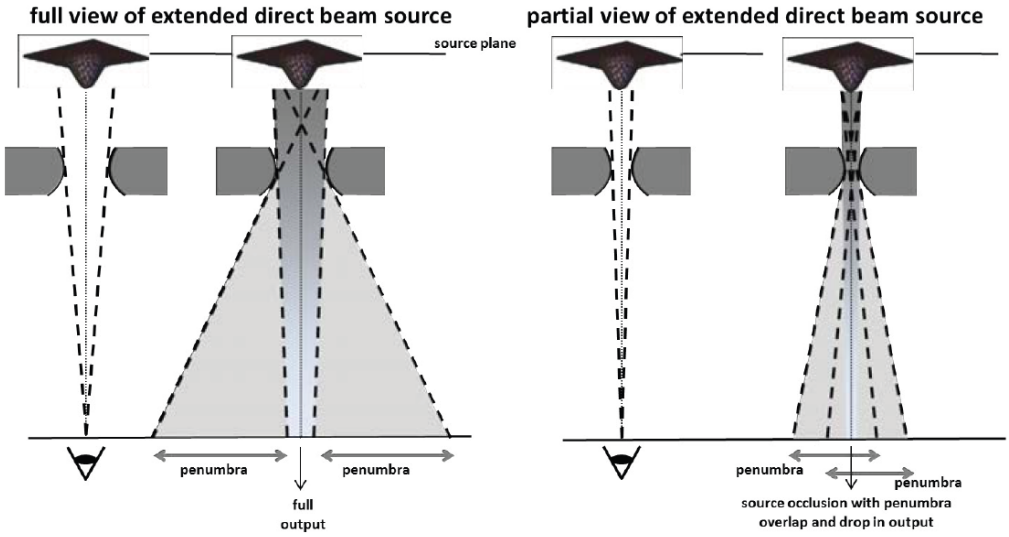

Figure 2.1: Schematic representation of full (left) and partial (right) source visibility in small photon fields. Partial occlusion of the primary photon source by the collimating system leads to a decrease in beam output and an extension of the penumbra. Adapted from IAEA and AAPM [11].

Detector Size and Perturbation Effects

In small field conditions, the dimensions of the detector relative to the beam are a critical factor in dose measurement accuracy. Larger-volume detectors, such as standard ionization chambers, suffer from volume averaging and beam perturbation, especially in high-gradient regions[11]. Even miniature detectors - such as diodes, micro-chambers, and plastic scintillators - present some trade-offs due to their energy and angular dependence.

2.3 Independent Dose Calculation in PSQA

Independent Dose Calculation (**IDC**) represents a critical element in Patient-Specific QA framework. Its primary purpose is to independently verify the dose distributions calculated by the TPS, thus providing a precaution against both systematic and random computational errors that could compromise treatment quality and patient safety [12] [13].

The IDC procedure typically begins with the extraction of essential treatment parameters from the TPS, including beam geometries, monitor unit values, and anatomical datasets such as CT scans. These data are then processed using a dose calculation algorithm that differs from the one implemented in the TPS. The ideology behind this methodological independence is to eliminate any inherent correlation

between the two systems, thereby maximizing the ability to detect discrepancies in dose computation [12].

Common IDC algorithms include analytical formalisms, fluence-based models, and Monte Carlo simulations, each offering a different balance between computational speed and dosimetric fidelity [12] [13].

Unlike measurement-based verification techniques, IDC is a purely computational approach. As such, it offers a more efficient and adaptable solution for high-throughput clinical environments. However, it also introduces limitations: IDC does not account for uncertainties related to beam delivery, mechanical performance of treatment units, or patient-specific anatomical variations occurring during therapy sessions [9].

For this reason, the AAPM Task Group 218 emphasizes that IDC should not be viewed as a replacement for measurement-based QA, but rather as a complementary tool that enhances overall verification robustness [9]. Similarly, Task Group 219 offers formal recommendations for the implementation of IDC in clinical practice, including guidelines for tolerance thresholds, validation procedures, and integration strategies with existing QA workflows [13].

When employed in conjunction with physical dosimetry techniques, IDC contributes to a multilayered QA protocol capable of detecting a broader spectrum of potential errors. This integrated approach, which may combine IDC with EPID-based dosimetry or detector arrays, has been shown to improve both the sensitivity and specificity of QA checks across various treatment modalities [9].

2.4 Dose Calculation Algorithms

The accuracy of dose calculation has long been a central concern in radiation therapy, especially as treatments become more conformal and patient-specific. Historically, dose calculations were performed manually at selected anatomical points to estimate monitor unit (MU) settings and guide treatment parameters. These early methods were inherently limited in scope, mainly depending on empirical correction factors and simple geometries that failed to model the complexities of photon interactions within heterogeneous patient tissues [14].

Advancements in computational power and imaging technologies have revolutionized the field, enabling three-dimensional dose calculations that include tissue inhomogeneities and account for primary and scatter radiation components. This evolution has significantly improved the accuracy and reliability of dose delivery, leading to improved tumor control and reduced toxicity to surrounding normal tissues [15].

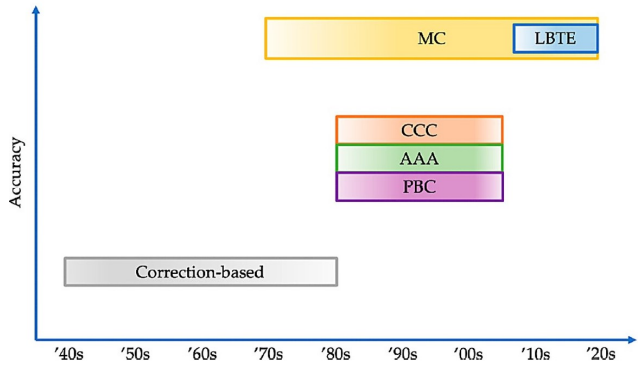

Figure 2.2: Historical evolution of dose calculation algorithms in external radiotherapy: from correction-based methods to Monte Carlo and Linear Boltzmann Transport Equation (LBTE) models. Adapted from De Martino et al. [16].

At the core of modern dose computation lie several mathematical frameworks, each balancing computational efficiency and physical accuracy. Analytical models such as the *Pencil Beam* approach rely on measured depth-dose data and correction factors, offering fast computation but less accuracy in complex geometries. Convolution and Superposition algorithms advance upon this by incorporating energy deposition kernels derived from Monte Carlo simulations, enabling more accurate modeling of scatter contributions and lateral electron transport [15] [14]. Figure 2.2 shows the evolution of dose calculations algorithms, emphazizing that each method differs in its computational efficiency, precision and clinical applicability.

Monte Carlo simulations represent the gold standard in dose modeling, as they explicitly simulate particle transport through stochastic methods based on physics' *first principles*. While these models are capable of achieving high fidelity, particularly in heterogeneous regions or small fields, their clinical application remains restricted by computational requirements, despite recent advancements in processing capabilities. The **Linear Boltzmann Transport Equation** (**LBTE**) is also gaining popularity as a potentially scalable alternative to Monte Carlo with equally high accuracy [14].

In highly modulated techniques is particularly important to take into consideration the clinical significance of dose calculation accuracy. Indeed, even small deviations can lead to $20 - 30\,\%$ changes in tumor control probability (TCP) or normal tissue complication probability (NTCP) [15] [14]. Therefore, ensuring dose accuracy is a critical component of PSQA and overall treatment quality.

Monte Carlo Algorithm

Monte Carlo (**MC**) techniques are employed in radiation dosimetry to simulate the stochastic transport of radiation within a medium of arbitrary composition and geometry. These methods rely on fundamental physical laws to probabilistically

model each interaction event, using tabulated interaction cross-sections for processes such as photoelectric effect, Compton scattering, and pair production [17]. An MC simulation code typically consists of four essential components [17]:

- a database of cross-section data for all considered interactions;
- transport algorithms that govern how particles propagate and interact within the medium;
- a detailed description of the geometry through which particles are tracked;
- statistical routines for analyzing output quantities of interest, such as energy deposition and dose.

Each particle history is simulated independently, and a large number of such histories are required to achieve statistically consistent results. The strength of MC methods lies in their ability to accurately account for complex geometries and inhomogeneous materials.

Chapter 3

Materials and Methods

3.1 Aim of the Study

The present chapter aims to provide a description of the materials, procedures, and methodologies employed throughout the study, which was carried out within the Medical Physics Unit of the AUSL-IRCCS in Reggio Emilia, Italy. The design of this work was inspired by a previous study conducted by Sceni et al. [18].

The purpose of the study was to evaluate and validate the Monte Carlo dose calculation module implemented in the commercial software RadCalc® (Lifeline Software Inc.), specifically focusing on the **Additional Radiation to Light Field Offset** (**ARLFO**) parameter. This parameter plays a crucial role in modeling the dosimetric characteristics of the multileaf collimator (MLC), and it corresponds to the Dosimetric Leaf Gap (DLG) parameter commonly used in Treatment Planning Systems (TPS) for linear accelerators provided by Varian Medical Systems (Palo Alto, CA, USA).

With the growing complexity of treatment techniques such as IMRT and VMAT, secondary independent dose calculations (IDCs) represent a critical step in detecting potential discrepancies between the planned and the delivered dose distributions; for this purpose, an increasing need for robust and efficient tools for IDC in the context of Patient-Specific QA is required. The aforementioned software **RadCalc** is widely used in clinical environments, and with its **Monte Carlo module** (**RCMC**) allows for more advanced and accurate dose recalculations compared to the other usually employed algorithms in clinical practice, such as Collapsed Cone Convolution-Superposition.

In the current study, an optimal ARLFO value for 6 MV photon beams (6X) was determined using an analytical and measurement-based methodology. A systematic and comparative analysis was conducted between point dose measurements acquired

with an independent ionization chamber placed at the central axis position (CAX) inside a dedicated water phantom and those calculated by RCMC. The percentage dose difference was analyzed as a function of the ARLFO parameter, allowing the identification of the relationship between the two quantities and thus the evaluation of the optimal ARLFO value. The test dataset employed in this work consists of 26 IMRT clinical plans - involving different tumour sites - delivered within the Radiotherapy Unit at AUSL-IRCCS, Reggio Emilia, Italy.

3.2 Software

3.2.1 Treatment Planning System (TPS)

The **Treatment Planning System** (**TPS**) employed in this study was Eclipse® (Varian Medical Systems, Palo Alto, CA, USA), which is the one commonly used at the Medical Physics Unit of AUSL-IRCCS in Reggio Emilia for clinical planning of photon beam radiotherapy. An example of the TPS view is reported in Figure 3.1.

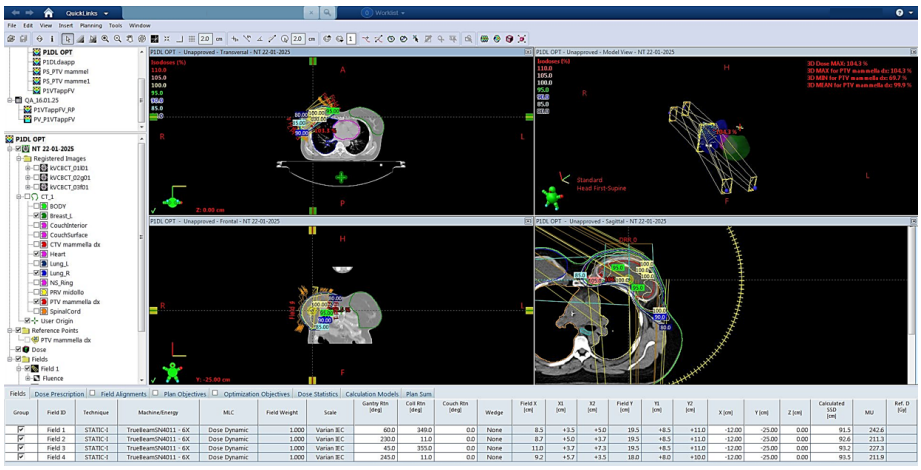

Figure 3.1: Illustration of a treatment plan in Eclipse® (Varian Medical Systems, Palo Alto, CA, USA)

Treatment plans were created using either Anisotropic Analitical Algorithm (AAA) or Acuros XB (AXB) algorithm - which are Eclipse dose calculation algorithms ([19]) - selected based on anatomical site and the complexity of the dose distribution. Specifically to this work, Eclipse was used to create IMRT plans, including beam geometry and MLC sequencing. Dose distributions calculated in Eclipse were exported in DICOM format to RadCalc and served as the reference for independent dose verification. All plans considered in this study were generated with a 6 MV photon beam and clinically commissioned beam models. The treatment geometry, dose

calculation grid resolution, and relevant plan parameters were selected according to institutional protocols and reflect standard clinical practice.

3.2.2 RadCalc 3D Monte Carlo

As already introduced in previous sections, **RadCalc®** (version 7.3, Lifeline Software Inc., Austin, TX, USA) is a commercial platform designed for secondary dose verification in external beam radiotherapy. It enables independent dose calculation and analysis through the import of DICOM RT plans generated by the TPS, CT images, and structure sets. RadCalc includes several calculation modules, such as EPID Dosimetry, Collapsed Cone Convolution Superposition (CCCS), Monte Carlo, and Treatment Log File Analysis, each designed to support different verification strategies depending on clinical needs. In the present study, the focus is on the Monte Carlo module, which allows for high-precision dose calculations based on beam-specific commissioning data and machine modeling.

Monte Carlo model is configured using a specific set of commissioning measurements, following institutional protocols. A configuration file containing dosimetric data for a given photon beam energy is imported into the software to initialize the RCMC engine. The system requires input of machine-specific parameters, and the software algorithm automatically optimizes internal variables such as spot size and mean energy, using the loaded dosimetric dataset as a reference. These datasets include measured Percentage Depth Dose (PDD) curves and Off-Axis Ratio (OAR) profiles, acquired in water phantoms under standardized conditions. This configuration process ensures that the Monte Carlo simulations are customized to the precise beam characteristics of the clinical linear accelerator, thereby enhancing the accuracy and clinical reliability of the dose verification process.

The software also enables some analysis such as γ index evaluation and point dose and dose profile comparisons. An illustration of the software interface is reported below in Figure 3.2

3.2.3 Introduction to Verisoft software

VeriSoft® (PTW Freiburg GmbH, Germany) is a dedicated software used in clinical practice for Patient-Specific QA in radiotherapy. It is intended to compare measured dose distributions with those computed by a treatment planning system or by independent verification software, such as RadCalc. The comparison is typically performed using the gamma index analysis, which evaluates both the dose difference and the spatial agreement between two dose distributions according to specific criteria.

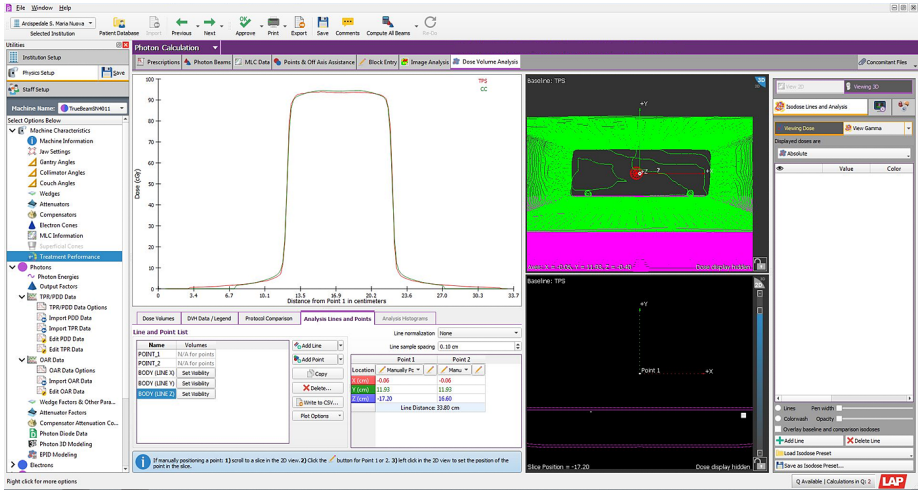

Figure 3.2: Example of a comparison between two dose distributions using the Analysis Lines and Points tab in RadCalc.

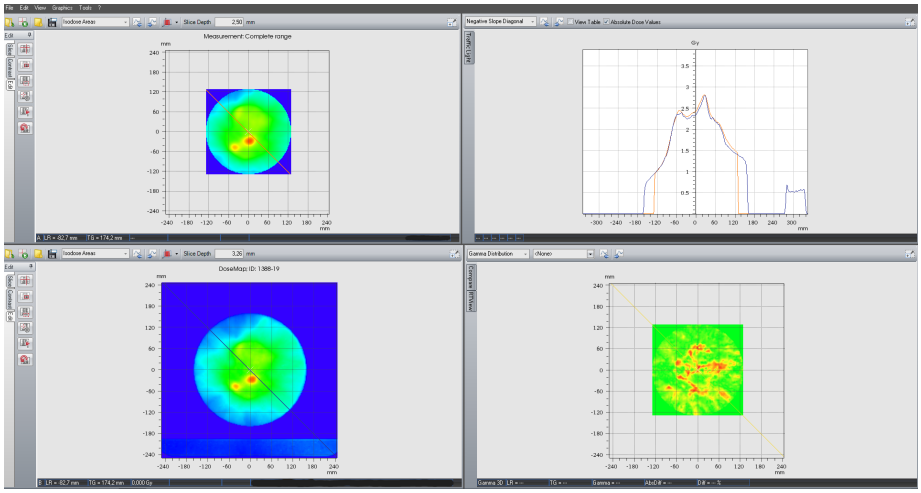

Figure 3.3: Example of Verisoft's graphical interface, illustrating the visualization of dose distributions and gamma index maps.

An example of Verisoft's graphical interface is shown in Figure 3.3. As can be noticed, It enables a visual examination of dose differences and gamma maps, facilitating the identification of spatial patterns in discrepancies. Its integration with specific measuring systems, and compatibility with DICOM-RT data, renders it a robust and versatile tool for PSQA in modern radiotherapy departments.

3.3 OCTAVIUS 4D

One of the most used specific measuring systems - referred to in 3.2.3 - is the OCTAVIUS 4D system (PTW, Freiburg, Germany). It is a highly accurate dosimetric phantom developed for PSQA in intensity-modulated radiation and volumetric-modulated arc therapies, and it consists of a cylindrical polymethyl methacrylate (PMMA) phantom mounted on a motorized rotational platform that synchronizes with the linac gantry movement during the delivery of the treatment plan. This arrangement guarantees that the radiation beam is always perpendicular to the detector surface at all gantry angles, facilitating precise reconstruction of dynamic dose delivery in rotational techniques. The phantom - represented in Figure 3.4 - has a diameter of 32.0 cm, a length of 34.3 cm, and a total weight of 49,0 kg [20].

(a) OCTAVIUS cylindrical phantom used for patient-specific QA measurements.

(b) Detector 1500 panel view inserted into the phantom.

Figure 3.4: OCTAVIUS 4D water-equivalent phantom.

Depending on the treatment type and the spatial resolution required, the OCTAVIUS 4D system can support different detector panels, such as the Detector 1500 for conventional IMRT/VMAT plans or the 1000^{SRS} for stereotactic applications. In this study, the Detector 1500 array was used.

During irradiation, the phantom acquires dose measurements at the central axis chamber of the detector matrix placed inside it. Those doses are subsequently reconstructed into a 3D dose volume - using the accompanying VeriSoft® software - and used as the reference dose. Then they are compared to the doses calculated either by TPS or RCMC for the same beam geometry, enabling gamma index analysis, isodose comparison, and dose profile evaluation. For these purposes, OCTAVIUS 4D

is widely adopted in clinical practice and represents a reliable tool for verifying the accuracy of complex treatment plans prior to patient delivery.

3.4 Gamma Index Analysis

The **gamma (γ) index analysis** is a quantitative method used to compare a measured dose distribution with a calculated one [21]. It accounts for both dose difference (ΔD) and spatial displacement (Δd), making it suitable for QA in IMRT and VMAT treatments, where steep dose gradients and spatial accuracy are critical. The metric is defined in an $(n+1)$-dimensional space, combining n spatial dimensions with one dose dimension, and expresses the minimum normalized distance between each point in the reference distribution and the evaluated distribution.

Mathematically, for each point $\vec{r}$ in the reference distribution, the gamma index is defined as:

$$\gamma(\vec{r}) = \min_{\vec{r}_e} \Gamma(\vec{r}_e, \vec{r}) \tag{3.1}$$

where Γ is the normalized distance between a reference point $\vec{r}$ and an evaluated point $\vec{r}_e$, calculated as:

$$\Gamma(\vec{r}_e, \vec{r}) = \sqrt{\left(\frac{||\vec{r}_e - \vec{r}||}{\Delta d}\right)^2 + \left(\frac{D(\vec{r}_e) - D(\vec{r})}{\Delta D}\right)^2} \tag{3.2}$$

Here, $D(\vec{r})$ and $D(\vec{r}_e)$ represent the dose at the reference and evaluated points, respectively. If $\gamma(\vec{r}) \leqslant 1$, the point is considered to pass the test.

In this study, gamma analysis was performed using the VeriSoft® software.The results are expressed in terms of the **Gamma Passing Rate** (**GPR**), defined as the percentage of points within the evaluated volume for which $\gamma \leqslant 1$. A **GPR** above 90% is generally considered clinically acceptable [22].

3.5 Verification of the RCMC performance

As the first step of this thesis work, the validation of the Monte Carlo dose calculation module integrated in RadCalc was performed following the protocol developed by the **RadCalc Italian Users Consortium** (**RIUC**), of which the AUSL-IRCCS of Reggio Emilia is both a member and promoter [23]. The consortium aims to promote the standardization of independent dose verification procedures through a structured and clinically applicable methodology within the use of RadCalc. The protocol is inspired to the work of Esposito et al. [24] and includes some elements from the "ESTRO 2023 recommendations for EPID in vivo dosimetry" adapted

to algorithmic validation. Although originally conceived for multiple verification systems, this framework was applied here exclusively to assess the performance of the Monte Carlo module integrated in RadCalc.

(a) (10 cm water-equivalent slab phantom setup.

(b) (a) 30 cm water-equivalent slab phantom setup.

Figure 3.5: Illustration of homogeneous slab phantom configurations. The setups represent the 10 cm and 30 cm thicknesses used for basic dosimetric validation under uniform conditions.

The validation tests were carried out considering different photon beams energies. Coherently to the purpose if this study, only the 6X energy is taken into account. The assessment included algorithmic performance in both homogeneous and inhomogeneous conditions, employing water-equivalent slab phantoms with standardized irradiation geometries. In the homogeneous setup (Figure 3.5), phantoms with thicknesses of 10 cm and 30 cm were irradiated with square open fields of 2x2 cm^2, 5×5 cm^2, 10×10 cm^2, and 20×20 cm^2, with the isocenter placed at the center of the phantom. Treatment plans were created in the TPS using Acuros XB, and the corresponding dose distributions were recalculated in RadCalc using the 3D photon Monte Carlo module, with a 2 mm dose grid resolution to ensure precise spatial sampling, particularly important for small fields.

To evaluate the algorithm's behavior in the presence of low-density inhomogeneities, additional tests were performed using slab phantoms incorporating internal air cavities. Two configurations were examined: one with a 2 cm air gap and another with a 5 cm air gap, with the isocenter positioned 2 cm beyond the interface between water-equivalent material and the air cavity. Figure 3.6 reports a schematic illustration of these scenarios, which has been designed to replicate anatomical het-

erogeneities encountered in thoracic or head-and-neck regions. For each setup, the same square field geometries used in the homogeneous tests were delivered.

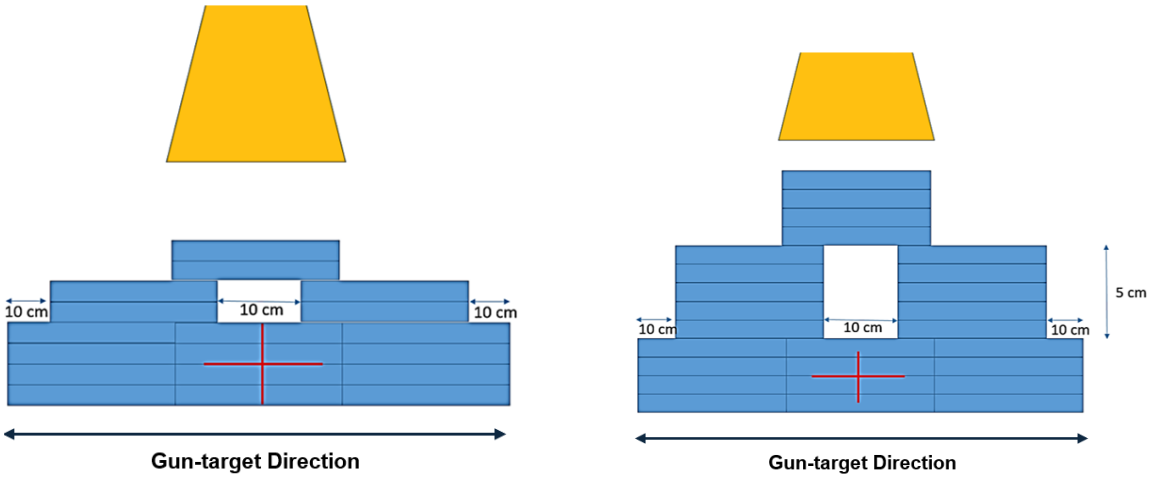

(a) 2 cm air gap phantom setup. **(b)** 5 cm air gap phantom setup.

Figure 3.6: Schematic representation of inhomogeneous slab phantom configurations. These setups were employed to simulate dose reconstructions in the presence of air gaps, representing anatomical inhomogeneities.

A quantitative evaluation was performed by calculating the percentage dose difference at the isocenter (ΔD_{iso}) and by conducting a 3D gamma index analysis. Gamma passing rates (GPRs) were computed using RadCalc and applying a global criterion of 3%/2 mm, with a 30% dose threshold relative to the reference distribution, in accordance with the protocol of Esposito et al..

The comparison between the Monte Carlo calculations and TPS dose distributions allowed for a detailed and systematic characterization of the accuracy, reproducibility, and clinical reliability of the independent model. The results of this validation process will be presented in the following chapter.

3.6 Methodology for ARLFO optimization in RCMC dose verification

Before the clinical validation phase, a systematic procedure was implemented to identify the optimal value of the **Additional Radiation to Light Field Offset** (**ARLFO**) parameter for Monte Carlo dose calculations in *RadCalc*. The aim was to tune this machine-specific parameter to improve the agreement between the independently calculated dose and the measured dose acquired during quality assurance procedures. The optimization focused exclusively on 6 MV photon beams (6X) and

was performed using the RadCalc Monte Carlo module, in conjunction with the Eclipse treatment planning system and a standard measurement setup.

The procedure began by selecting seven static test plans, each defined by a fixed MLC aperture: 2 mm, 4 mm, 6 mm, 10 mm, 14 mm, 16 mm, and 20 mm. These plans were created in Eclipse, where the reference dose distributions were calculated using AXB algorithm. Each plan was then delivered on a water phantom using the Varian TrueBeam STx linear accelerator (TrueBeam) operated at the Radiotherapy Unit of AUSL-IRCCS, Reggio Emilia, Italy (Figure 3.7). A 6X photon beam was used throughout all irradiations. For each of the aforementioned plan (from 2 mm to 20 mm), a point dose measurement was acquired using an ionization chamber placed at the central axis (CAX) within the phantom, thus providing the measured dose for each configuration.

Figure 3.7: Illustration of the Varian TrueBeam STx linear accelerator in use at the Radiotherapy Unit, AUSL-IRCCS, Reggio Emilia, Italy.

Meanwhile, the same plans were exported from Eclipse to RadCalc via DICOM RT format. The purpose was to independently recalculate the dose at the same measurement point using the Monte Carlo engine. A custom workflow was followed for each plan to assess the impact of different ARLFO values on the calculated dose. Before each RCMC simulation, the ARLFO parameter was modified directly in RadCalc via the following path:

> `Utilities` → `Photons Modeling` → Selection of the machine model (TrueBeam) → Energy selection (6X) → ARLFO input → Model Commissioning → `Save`.

The starting point for all tests was the default value ARLFO = 0 cm. After each modification, the RCMC simulation was run for the current plan using specific

computational settings, such as a dose grid spacing of 2 mm (*Fine grid*), and predefined CT-density conversion tables, to ensure high-resolution sampling of small field configurations. An example of the RadCalc tab is shown below in Figure 3.8.

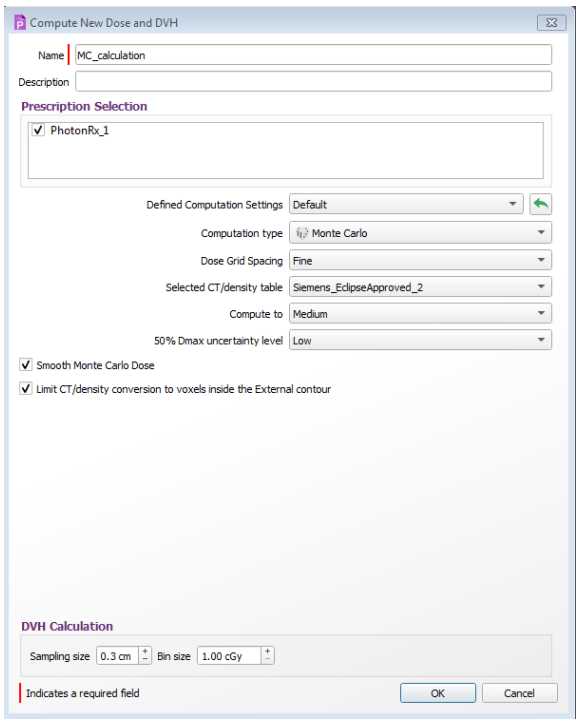

Figure 3.8: Example of the RadCalc Monte Carlo computation interface used to perform RCMC simulations. The tab shown includes settings such as the *Fine* dose grid spacing, and a specified CT/density table.

For each plan, the calculated dose at the CAX point was extracted and compared against the corresponding measured dose. The percentage dose difference ($\%\Delta D$) between the two was computed as:

$$\Delta D\% = \frac{D_{\text{calc}} - D_{\text{meas}}}{D_{\text{meas}}} \times 100$$

The process was then repeated for six additional ARLFO values, chosen iteratively on the basis of preliminary results to minimize the discrepancy between calculated and measured doses. For each MLC field, a dose difference as function of ARLFO curve was plotted. A linear fit was then applied to model the relationship, and the optimal ARLFO parameter was extracted as the value corresponding to a zero dose difference, i.e., the point where RCMC calculation matches the measurement at the CAX.

As a result, seven optimal ARLFO values were obtained, one for each of the selected field sizes. It was observed that the influence of ARLFO on the calculated

dose was more significant for smaller fields, while its effect was progressively reduced for larger apertures. To derive a single representative value of ARLFO to be used in clinical configuration, a weighted average was computed, in which each optimal ARLFO was weighted based on the absolute value of the average percentage dose differences observed for that field. This approach inherently assigns more weight to small fields, where sensitivity to ARLFO is higher, and less to larger fields, where - as previously said - the impact is less critical. The resulting weighted ARLFO value was then considered as the optimal parameter for subsequent clinical validation.

3.7 Validation of the Optimal ARLFO Parameter

Following the parameter optimization process described in the previous section, a second phase was carried out to validate the effectiveness of the optimal ARLFO value. The aim of this validation was to demonstrate that using the optimal ARLFO parameter leads to an improvement in the agreement between the measured and RCMC-calculated dose distributions when compared to the default null-ARLFO configuration.

To this end, a test set of 26 clinical IMRT plans was selected, all computed with 6X photon beams. These plans covered a range of anatomical treatment sites and were distributed as follows: 8 breast, 7 lung, 8 head-and-neck, and 3 brain cases. All plans were delivered using the TrueBeam linear accelerator, the same employed in the tuning phase.

Each clinical plan was exported from Eclipse and recalculated in RadCalc using the RCMC module under two different configurations:

- the standard configuration, with ARLFO = 0 cm, and
- the optimal configuration, using the weighted average ARLFO value derived from the procedure explained in section 3.6.

RCMC calculations were then exported to a selected folder, in order to be subsequently analyzed.

To perform a quantitative comparison, each plan was also processed in VeriSoft® software. After importing the treatment plans, for each of these, the 3D dose distribution reconstructed from measurements was compared to the RCMC-calculated dose using both ARLFO configurations. The comparison was performed using gamma index analysis, with two criteria applied:

- 3%/2 mm with a 10% global dose threshold [9], and
- 3%/3 mm with a 50% local dose threshold, focusing on high-dose target regions.

This procedure was repeated for all 26 clinical plans. The resulting gamma passing rates were used to assess the potential dosimetric advantage offered by the optimal ARLFO value.

The overall workflow adopted in this study for IMRT dose verification is summarized below in Figure 3.9.

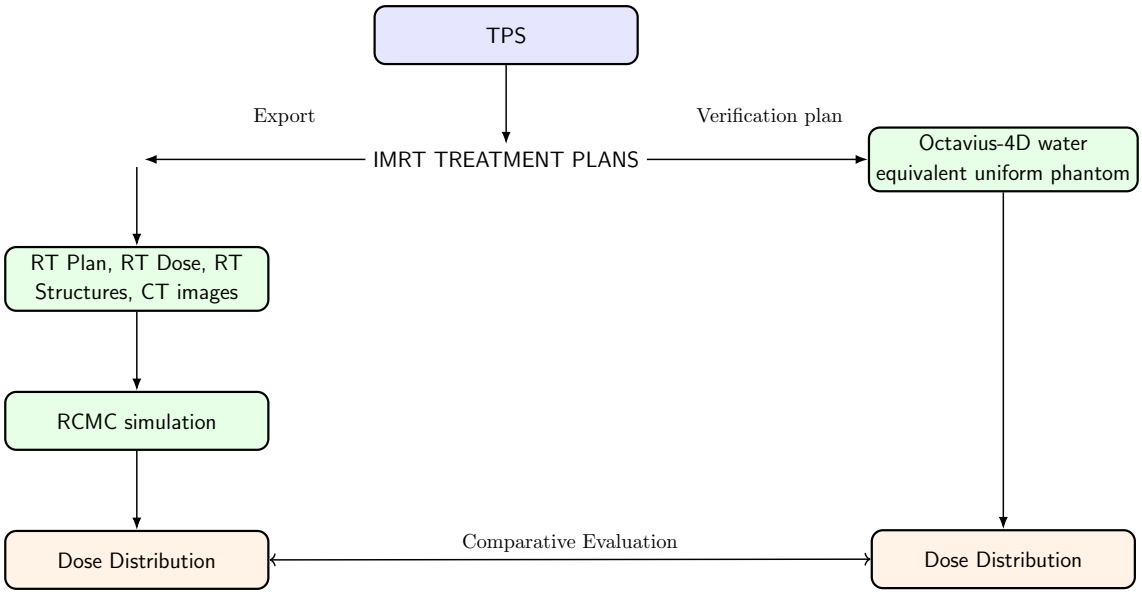

Figure 3.9: Workflow of dose comparison using RCMC simulation and phantom-based measurements.

3.8 Extraction of MLC relevant parameters from Clinical Plans

An in-house MATLAB script was used to extract beam-specific metrics from each DICOM RP-Plan file. This in-house tool was designed to retrieve MLC-related parameters relevant to the analysis, including the median leaf pair aperture and the percentage of MLC apertures below 4 mm for each modulated field.

These data were collected to support further interpretation of the validation results, particularly in relation to the field-size dependence of the ARLFO parameter. Since the optimization method was analytically derived using a weighted approach that emphasizes smaller field sizes, the expectation was to observe a significant improvement in gamma passing rates when applying the optimal ARLFO value, especially in plans characterized by more narrow MLC apertures.

3.9 Statistical Analysis

To quantitatively assess the improvement in dose agreement following the ARLFO optimization, a statistical analysis was performed on the gamma index results obtained from the validation set. The goal was to determine whether the optimal RCMC configuration led to a statistically significant enhancement in GPRs, compared to the standard configuration with ARLFO set to 0 cm.

Given that each clinical plan was evaluated under both configurations, the resulting dataset consisted of paired gamma values, one per configuration, per plan. A **Wilcoxon signed-rank test** was selected as a non-parametric statistical alternative to employ. This test is specifically designed to assess whether the median of the differences between paired samples significantly deviates from zero.

The test was applied separately for each of the gamma analysis criteria adopted in this study:

- 3%/2 mm with a 10% global dose threshold;
- 3%/3 mm with a 50% local dose threshold

This approach ensures a statistically consistent evaluation of the optimization process, aligning with methods commonly used in clinical validation studies.

A detailed interpretation of the results is presented in the next chapter, where p-values are reported along with the observed GPR differences. The analysis paves the way for the idea that implementing the optimized ARLFO configuration can improve the agreement in independent RCMC dose calculations.

Chapter 4

Results and Discussion

4.1 Preliminary validation of RCMC against TPS: Analysis on open square fields

As introduced in section 3.5, the initial phase of the study focused on the validation of the RCMC dose calculation algorithm compared to TPS performance, considering both its AXB and AAA algorithms. The results for percentage dose differences at the CAX point between TPS and RadCalc's Monte Carlo engine are collected in table 4.1 and discussed below.

Phantom type	**RCMC vs AXB**	**RCMC vs AAA**
Homogeneous	(-0.3 ± 1.3)%	(-0.9 ± 1.5)%
Inhomogeneous	(-2.1 ± 1.6)%	(-4.8 ± 0.9)%

Table 4.1: Average point dose differences at CAX between RCMC and TPS' algorithms (AXB and AAA) for open square fields in homogeneous conditions

A significant trend can be observed across phantom configurations. Results in homogeneous conditions show a consistent agreement between RCMC and the TPS algorithms. Specifically, an average dose difference of -0.3% confirms the compatibility between these two dose algorithms, as expected. Similarly, the discrepancy with AAA remains moderate (-0.9 ± 1.5)%, though slightly more pronounced, as expected given how the AAA algorithm works.

In contrast, once considering inhomogeneous conditions a more significant divergence occurs, particularly in the comparison with AAA. The average deviation between RCMC and AXB increases to –2.1%, reflecting a higher computational complexity of modelling low-density or interface regions. The difference with AAA becomes more important, reaching a discrepancy of 4.8%, and highlights the reduced

accuracy of AAA in non-homogeneous media, where the algorithm's assumptions no longer hold. Notably, the lower standard deviation observed in this configuration suggests a systematic underestimation by AAA in the presence of inhomogeneities, whereas the broader spread in the AXB results may be attributed to its more detailed physical modelling and sensitivity to geometry. This suggests the importance of algorithm selection in patient-specific dose verification, particularly when patient's anatomical variability plays a non-negligible role.

To evaluate the spatial and dosimetric agreement between RCMC and TPS dose distributions, Gamma index analysis was also performed. The analysis was conducted considering the 3%/2 mm global criterion, with 30% threshold, as suggested by Esposito et al. [24]. Results are presented in table 4.2.

Phantom type	**GPR**
Homogeneous	$(92 \pm 8)\%$
Inhomogeneous	$(67 \pm 15)\%$

Table 4.2: Average GPRs obtained with 3%/2mm, 30% threshold criteria between RCMC and TPS (AXB) dose distributions, for homogeneous and inhomogeneous phantoms.

In homogeneous conditions, RCMC exhibited a gamma passing rate of 92% across various open square fields, with a moderately high standard deviation σ_{homo}. While the overall result approaches clinical acceptance thresholds (typically 90%), the relatively high $\sigma homo$ indicates considerable variability across field sizes. This is particularly relevant in small-field configurations where factors such as electronic disequilibrium and detector size effects (see section 2.2) can affect dose agreement.

For the inhomogeneous-based comparison, the average gamma passing rate drops significantly to $(67 \pm 15)\%$. This suggests a reduced agreement between calculated and measured doses in low-density or heterogeneous regions, likely due to the challenges introduced by complex tissue interfaces. The large standard deviation observed in this group reflects substantial inconsistency across configurations, reinforcing the difficulty of accurate dose modelling in such contexts even for advanced algorithms like Monte Carlo. From a statistical perspective, the contrast in standard deviations is striking: while the homogeneous setup already presents non-negligible spread ($\sigma_{homo} = 8\%$), the inhomogeneous scenario almost doubles this value ($\sigma_{inhomo} = 15\%$).

This observation paves the way for a crucial point: mean values alone may not be sufficient to capture the clinical reliability of an algorithm, and the variability itself should be considered when assessing its robustness. These findings suggest that although RCMC performs well on average in uniform media, its predictive

accuracy in anatomically realistic conditions remains sensitive to field configuration, reinforcing the need for field-specific thresholds or complementary QA techniques.

4.2 Tuning of ARLFO parameter

A dedicated tuning method - as already described in section 3.6 - was performed by varying the ARLFO parameter, starting from the standard value of 0 cm. Tables from 4.3 to 4.9 report the results for each MLC aperture along with the corresponding graphs displaying the relationship between dose differences ΔD and ARLFO values.

MLC aperture	ARLFO (cm)	ΔD (%)
2 mm	0.000	26.4
	−0.010	21.2
	−0.047	4.70
	−0.060	−1.80
	−0.066	−3.30
	−0.068	1.00
	−0.163	−33.2

Table 4.3: Tuning data for 2 mm MLC aperture: variation of dose difference at CAX as a function of ARLFO value.

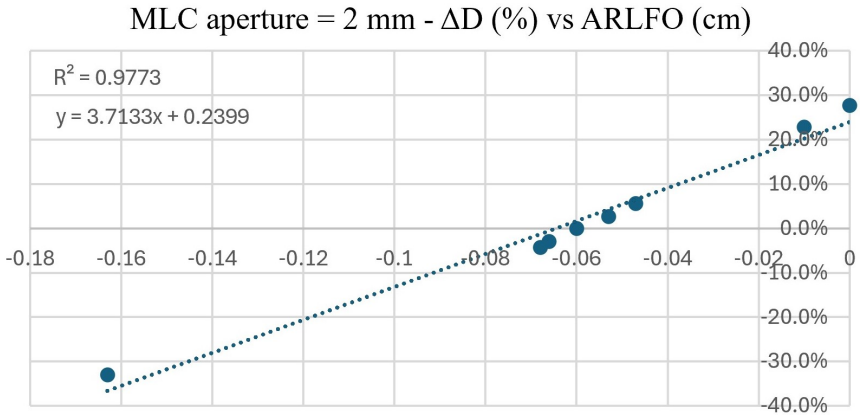

Figure 4.1: Tuning curve showing the dose difference at CAX as a function of ARLFO for the 2 mm MLC aperture.

MLC aperture	ARLFO (cm)	ΔD (%)
4 mm	0.000	23.3
	−0.010	19.8
	−0.047	6.40
	−0.060	1.90
	−0.066	−0.100
	−0.068	−0.600
	−0.163	−32.5

Table 4.4: Tuning data for 4 mm MLC aperture: variation of dose difference at CAX as a function of ARLFO value.

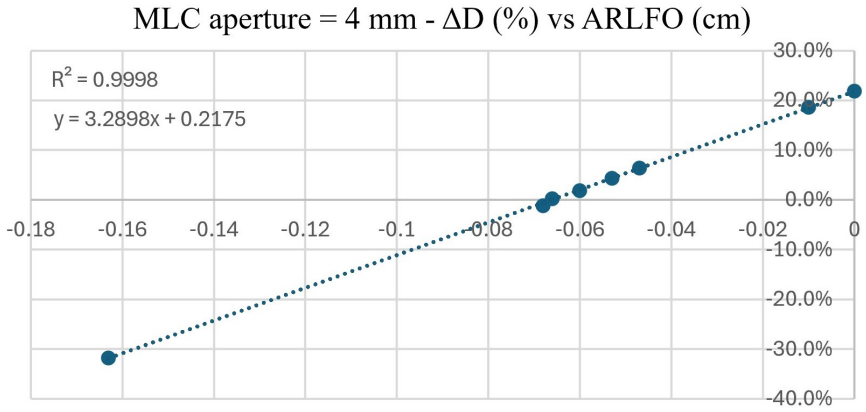

Figure 4.2: Tuning curve showing the dose difference at CAX as a function of ARLFO for the 4 mm MLC aperture.

MLC aperture	ARLFO (cm)	ΔD (%)
6 mm	0.000	16.6
	−0.010	14.2
	−0.047	6.40
	−0.060	3.50
	−0.066	0.900
	−0.068	0.200
	−0.163	−23.3

Table 4.5: Tuning data for 6 mm MLC aperture: variation of dose difference at CAX as a function of ARLFO value.

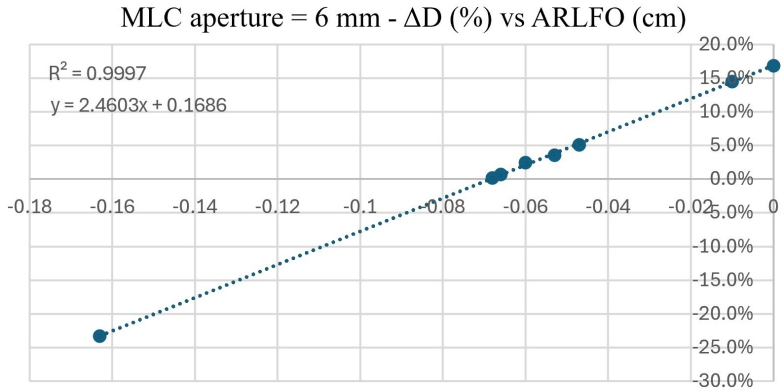

Figure 4.3: Tuning curve showing the dose difference at CAX as a function of ARLFO for the 6 mm MLC aperture.

MLC aperture	**ARLFO (cm)**	**ΔD (%)**
	0.000	6.00
	−0.010	5.50
	−0.047	−4.70
10 mm	−0.060	−3.50
	−0.066	−4.60
	−0.068	−4.70
	−0.163	−19.1

Table 4.6: Tuning data for 10 mm MLC aperture: variation of dose difference at CAX as a function of ARLFO value.

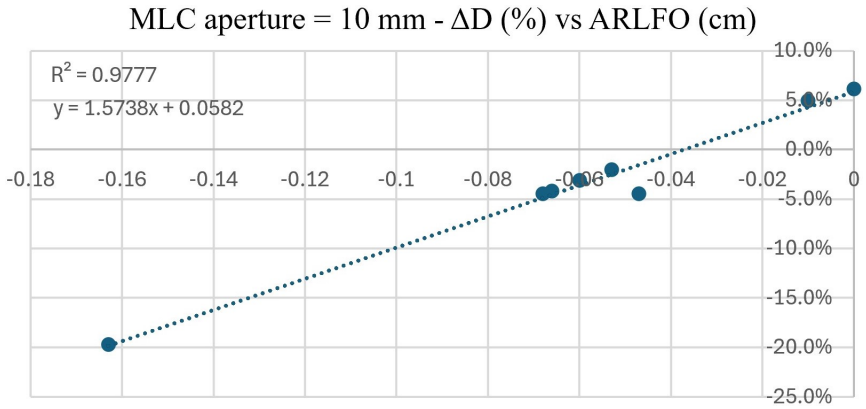

Figure 4.4: Tuning curve showing the dose difference at CAX as a function of ARLFO for the 10 mm MLC aperture.

MLC aperture	ARLFO (cm)	ΔD (%)
14 mm	0.000	3.20
	−0.010	2.20
	−0.047	−2.30
	−0.060	−4.60
	−0.066	−4.90
	−0.068	−4.60
	−0.163	−17.0

Table 4.7: Tuning data for 14 mm MLC aperture: variation of dose difference at CAX as a function of ARLFO value.

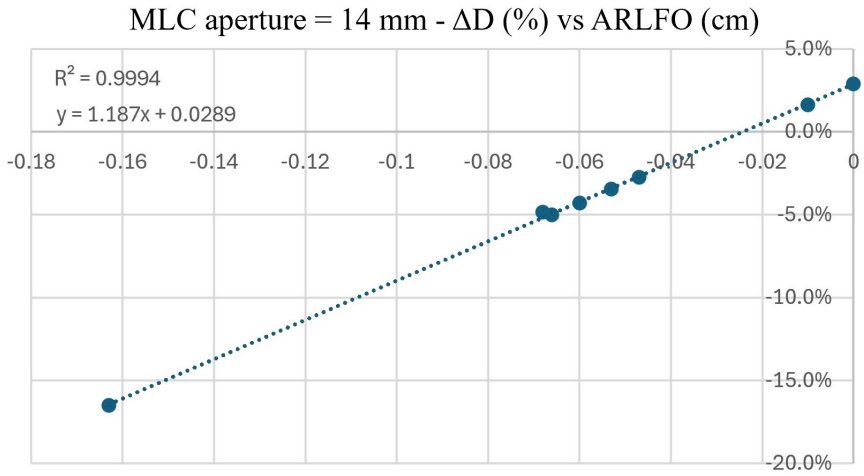

Figure 4.5: Tuning curve showing the dose difference at CAX as a function of ARLFO for the 14 mm MLC aperture.

MLC aperture	ARLFO (cm)	ΔD (%)
16 mm	0.000	1.80
	−0.010	2.20
	−0.047	−2.10
	−0.060	−3.60
	−0.066	−4.70
	−0.068	−4.60
	−0.163	−15.2

Table 4.8: Tuning data for 16 mm MLC aperture: variation of dose difference at CAX as a function of ARLFO value.

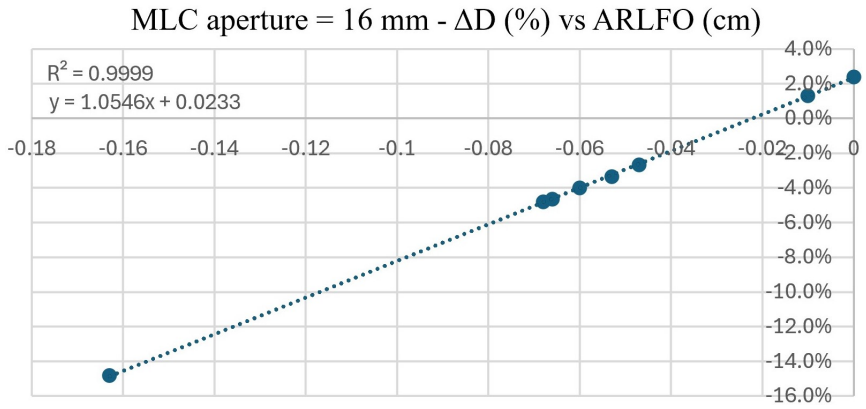

Figure 4.6: Tuning curve showing the dose difference at CAX as a function of ARLFO for the 16 mm MLC aperture.

MLC aperture	ARLFO (cm)	ΔD (%)
20 mm	0.000	2.40
	−0.010	2.60
	−0.047	−2.20
	−0.060	−3.20
	−0.066	−3.80
	−0.068	−4.20
	−0.163	−12.7

Table 4.9: Tuning data for 20 mm MLC aperture: variation of dose difference at CAX as a function of ARLFO value.

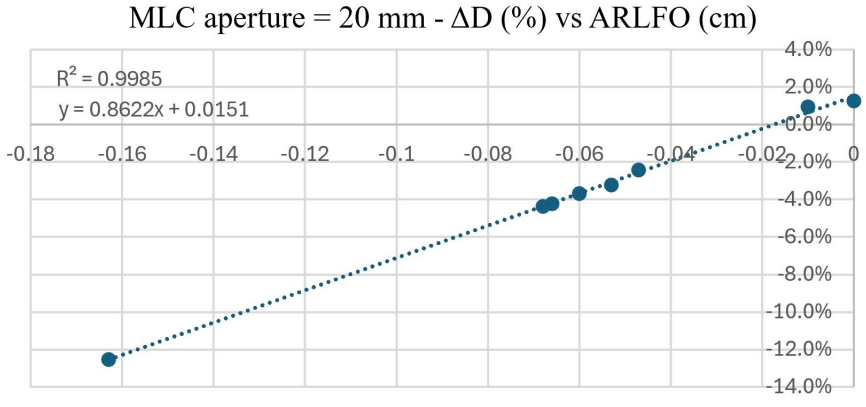

Figure 4.7: Tuning curve showing the dose difference at CAX as a function of ARLFO for the 20 mm MLC aperture.

MLC aperture (mm)	Slope	y-intercept	R^2
2	3.7133	0.2339	0.9773
4	3.2898	0.2175	0.9998
6	2.4603	0.1686	0.9997
10	1.5738	0.0582	0.9777
14	1.1870	0.0289	0.9994
16	1.0546	0.0233	0.9999
20	0.8622	0.0151	0.9985

Table 4.10: Linear regression parameters for each MLC aperture, including slope, y-intercept, and R^2 coefficient, based on the ARLFO tuning curves.

For each MLC aperture, a clear monotonic trend between the two variables is recognizable and confirmed by the application of a linear interpolation. Indeed, the latter returns a regression coefficient R^2 close to 1, emphasizing a strong linear correlation. For completeness, Table 4.10 reports the R^2 corresponding to each field aperture, along with other linear regression parameters.

MLC aperture (mm)	ARLFO value for $\Delta D = 0\%$ (cm)
2	−0.065
4	−0.066
6	−0.069
10	−0.037
14	−0.024
16	−0.022
20	−0.018
Optimal ARLFO parameter	**−0.053**

Table 4.11: Optimal ARLFO values extrapolated from linear fits for each MLC aperture. The final ARLFO parameter (−0.053 cm) was calculated as a weighted average, where the weighting factors correspond to the mean absolute percentage dose differences observed for each field.

From each linear plot, the ARLFO value corresponding to a zero percent dose difference was extracted analytically as the root of the fitted function. These values, summarized in Table 4.11, represent the optimal ARLFO parameter for each MLC aperture tested. In order to obtain a unique, clinically applicable parameter, a weighted average was calculated. The weighting factors were defined as the mean absolute dose differences observed for each field, assigning greater importance to

smaller apertures, which exhibit higher sensitivity to ARLFO variations. This approach ensures that the final value is driven by those configurations. The resulting optimal ARLFO value was **–0.053 cm**

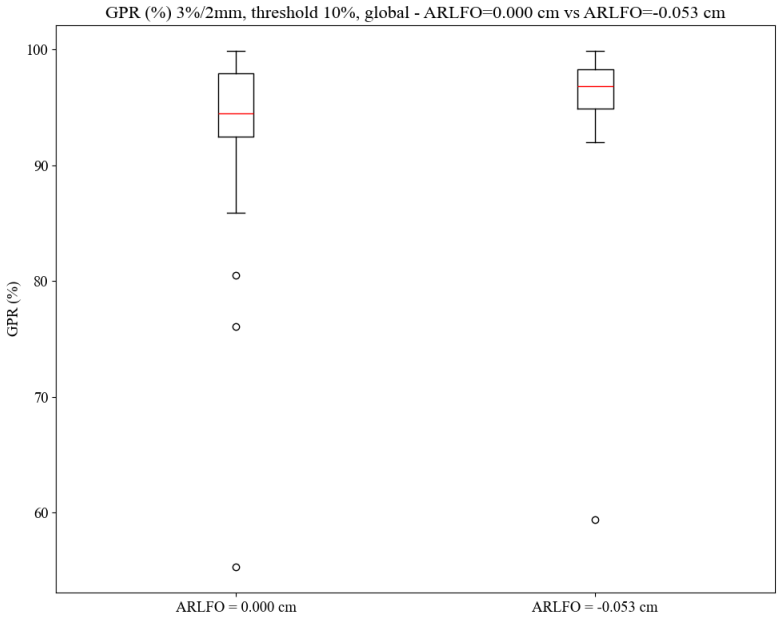

(a) GPR values using the 3%/2 mm criterion with a 10% global threshold.

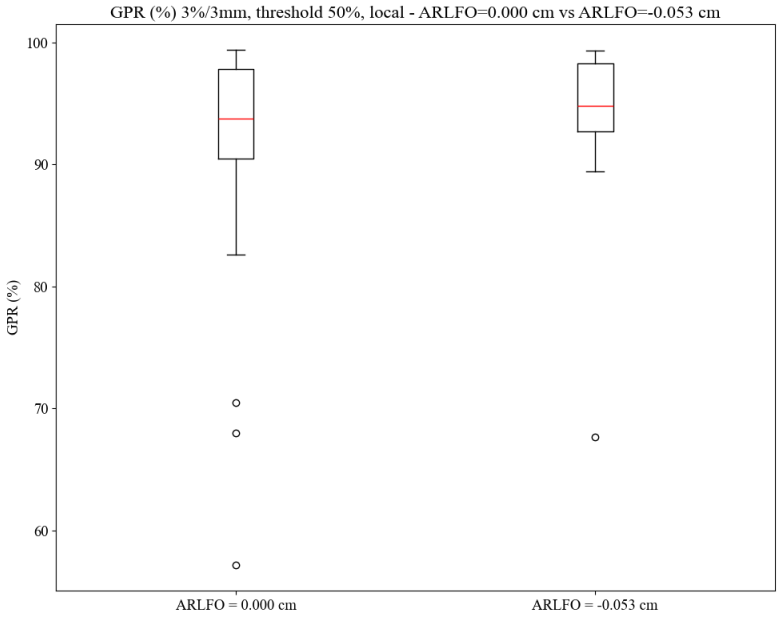

(b) GPR values using the 3%/3 mm criterion with a 50% local threshold.

Figure 4.8: Boxplots comparing the GPR distributions under two ARLFO configurations (0.000 cm and −0.053 cm), for different analysis criteria. In both cases, the optimal ARLFO setting improves the dosimetric agreement by increasing the median GPR and reducing the number of outliers.

4.3 Comparison between measured dose and RCMC calculation

To validate the performance of RCMC with different ARLFO configurations, a comparison study was conducted using 26 clinical treatment plans. The methodology adopted to assess whether the optimal parameter could improve the agreement between RCMC calculations and measured doses is described in Section 3.7. This section presents a discussion of the corresponding results.

Table 4.12 summarizes the dosimetric performance of the clinical plans evaluated with two ARLFO configurations using two gamma analysis criteria: 3%/2 mm with a 10% threshold (global evaluation) and 3%/3 mm with a 50% threshold (local evaluation). The data clearly indicate an overall improvement in GPR when shifting from ARLFO = 0.000 cm to ARLFO = −0.053 cm.

Although the improvement is not uniformly distributed, it is particularly consistent within the breast, head and neck, and brain treatment sites, suggesting that the optimal ARLFO configuration may have site-specific effects.

To support these findings, two boxplots were generated and are reported in Figure 4.8. These plots illustrate the distribution of GPR values for both ARLFO configurations.

Under the global criterion, the first boxplot demonstrates a clear upward shift in GPR for ARLFO = −0.053 cm, with a higher median and a reduction in negative outliers, indicating more robust and consistent performance. A comparable trend is evident for the local criterion, as the data corroborate this observation by exhibiting a narrower interquartile range and fewer low-end outliers.

4.4 Statistical Anlysis

To statistically assess whether the improvement in GPR observed with the optimal ARLFO configuration discussed in the previous section is significant, a **Wilcoxon signed-rank test** was performed. This non-parametric test was selected as it is appropriate for paired samples, according to the fact that each clinical plan yields two GPR values under different ARLFO settings.

Under the global criterion (3%/2 mm with 10% threshold), the Wilcoxon test returned a p-value of 0.0090, indicating a statistically significant difference between the two configurations. This result confirms that the optimal ARLFO setting yields a measurable and consistent improvement in dosimetric agreement when evaluated using global gamma analysis.

Conversely, for the local criterion (3%/3 mm with 50% threshold), the p-value was 0.1651, which does not reach the conventional threshold for statistical signifi-

cance (typically $\alpha = 0.05$). Although a trend toward improvement is still evident - particularly in the boxplot analysis and in individual cases presented in section 4.3 — the variability in the local criterion appears higher, possibly due to its stricter spatial normalization or increased sensitivity to dose gradients.

In the following section, the role of anatomical treatment sites in relation to the observed improvement in gamma passing rates will be further investigated.

4.5 Investigation of anatomical site influence

In the previous section, the Wilcoxon test performed for the 3%/3 mm with 50% threshold criterion did not yield to a significant statistical result. A closer inspection of the data (Table 4.12) suggests that the anatomical site of the treatment may influence the impact of ARLFO optimization. In particular, it can be observed that plans targeting the lungs tend to show lower GPR values when the doses comparison is computed considering ARLFO = -0.053 cm configuration.

To better quantify this observation, a Wilcoxon signed-rank test was repeated after excluding lung cases from the local gamma criterion dataset. Notably, the resulting p-value dropped to 0.0161, reaching statistical significance. This confirms that the improvement introduced by optimal ARLFO is consistent across anatomical sites, with lung plans representing an exception due to their underlying heterogeneity. This exception is consistent with the findings reported by Sceni et al. [18], who demonstrated that Monte Carlo-based models, when properly tuned, are particularly effective in identifying discrepancies in lung plans that standard QA methods may overlook. In accordance with their results, the thoracic region presents specific challenges for dose verification, and this could lead to the idea that improvements introduced by correction strategies like ARLFO may be less effective when anatomical complexity is not explicitly addressed.

4.6 Perspectives for Future Investigations

To further explore the variation in gamma passing rate improvements across anatomical sites, an additional analysis was performed based on specific MLC-related parameters. An in-house MATLAB script was developed to extract relevant dosimetric indicators directly from the DICOM RP-Plan files. As reported in Appendix A, the script prints, for each clinical plan, both the median MLC leaf opening and the percentage of apertures smaller than 4 mm, which serves as an indicator of the presence of small fields in highly modulated plans (see Chapter 2). The extracted values are summarized in Table 4.13, along with the ΔGPR between the two ARLFO configurations.

To explore potential correlations, scatter plots were generated showing ΔGPR values as a function of the percentage of MLC apertures smaller than 4 mm. However, these plots did not reveal any clear or statistically meaningful correlation between the frequency of small MLC apertures and the observed ΔGPR values, under either gamma analysis criterion.

Despite the lack of definitive results, this preliminary analysis paves the way for future investigations. Specifically, it highlights the potential value of studying how optimal ARLFO could interact with anatomical site characteristics and the prevalence of small field segments in highly modulated treatment plans. A more comprehensive analysis - potentially involving larger datasets - may uncover further clinically relevant patterns.

Plan	GPR (%) 3%/2mm 0.00 cm	GPR (%) 3%/2mm −0.053 cm	GPR (%) 3%/3mm 0.00 cm	GPR (%) 3%/3mm −0.053 cm	Anatomical site
1	92.1	96.3	88.5	92.6	Breast
2	80.5	94.7	70.5	96.5	
3	92.9	94.9	90.2	93.6	
4	96.7	97.9	94.3	96.6	
5	91.1	92.0	93.2	96.5	
6	94.3	97.1	92.6	94.4	
7	98.0	99.5	94.7	99.1	
8	93.8	96.6	90.6	98.1	
9	92.3	92.3	93.0	89.9	Lung
10	76.1	92.3	68.0	92.9	
11	96.3	95.0	96.3	89.4	
12	99.5	98.2	97.6	90.4	
13	97.8	95.2	98.1	92.5	
14	99.6	98.2	99.3	93.3	
15	94.1	97.8	93.0	94.1	
16	99.6	99.1	99.4	98.7	Head & Neck
17	97.5	99.3	97.9	98.7	
18	55.3	59.4	57.2	67.7	
19	95.7	95.0	97.4	95.0	
20	94.7	93.1	96.2	91.1	
21	93.2	98.1	91.9	98.8	
22	94.2	99.5	90.4	99.3	
23	85.9	95.2	82.6	96.0	
24	99.4	99.9	98.6	98.7	Brain
25	99.9	99.5	99.0	94.6	
26	98.5	98.3	98.1	98.3	

Table 4.12: Gamma passing rates for 26 clinical treatment plans, evaluated with two gamma criteria (3%/2mm with 10% global threshold and 3%/3mm with 50% local threshold), using both the default ARLFO configuration (0.00 cm) and the optimized value (−0.053 cm). Green highlights improvements, orange highlights degradations.

Plan	**ΔGPR (%) (3%/2mm)**	**ΔGPR (%) (3%/3mm)**	**median MLC gap (mm)**	**% gap < 4 mm**	**Anatomical site**
1	4.20	4.10	16.9	47.4	Breast
2	14.2	26.0	5.1	75.0	
3	2.00	3.40	18.8	50.5	
4	1.20	2.30	11.2	43.8	
5	0.90	3.30	0.5	57.6	
6	2.80	1.80	16.3	34.0	
7	1.50	4.40	15.9	49.4	
8	2.80	7.50	5.6	47.8	
9	0.00	-3.10	23.9	50.1	Lung
10	16.2	24.9	5.9	73.5	
11	-1.30	-6.90	25.8	54.8	
12	-1.30	-7.20	34.4	60.5	
13	-2.60	-5.60	24.1	64.2	
14	-1.40	-6.00	10.7	72.7	
15	3.70	1.10	26.9	63.0	
16	-0.50	-0.70	41.7	48.0	Head & Neck
17	1.80	0.80	27.8	50.2	
18	4.10	10.5	25.3	52.8	
19	-0.70	-2.40	22.4	41.5	
20	-1.60	-5.10	17.4	52.2	
21	4.90	6.90	13.7	49.7	
22	5.30	8.90	36.8	36.8	
23	9.30	13.4	22.7	40.1	
24	0.50	0.10	21.45	77.6	Brain
25	-0.40	-4.4	37.5	51.1	
26	-0.20	0.20	35.9	72.4	

Table 4.13: Summary of ΔGPR values for both gamma criteria, MLC median gap, percentage of small apertures, and anatomical site.

Chapter 5

Conclusions

This thesis work has focused on the optimization of **RadCalc's Monte Carlo calculation module** (**RCMC**), with a particular emphasis on the **Additional Radiation to Light Field Offset** (**ARLFO**) parameter. The principle aim was to tune this machine-specific parameter to enhance the agreement between independently calculated and measured dose distributions obtained during **Patient-Specific Quality Assurance** (**PSQA**) procedures, specifically for 6X beam energy.

The optimization process was conducted through an analytical approach based on the comparison of RCMC calculated and measured doses, using seven static test plans, each defined by a fixed MLC aperture ranging from 2 mm to 20 mm. Results indicated that the influence of ARLFO on the calculated dose is more pronounced for smaller field sizes. To define a representative value of ARLFO, a weighted average was computed, assigning greater importance to smaller fields. This evaluation yielded an optimal ARLFO value of –0.053 cm, which was subsequently employed for clinical validation.

A test dataset including 26 clinical treatment plans was then analyzed. For each plan, phantom-based measured doses were compared with RCMC-calculated ones, using both the standard ARLFO value of 0 cm and the optimal value of –0.053 cm. Agreement was assessed via gamma index analysis under two criteria: 3%/2 mm with a 10% global dose threshold, and 3%/3 mm with a 50% local dose threshold. A Wilcoxon signed-rank test was also performed and revealed a statistically significant improvement in agreement for the first criterion, though not for the second.

Further analysis suggested that the impact of ARLFO optimization may be influenced by the treatment site. In particular, lung plans tended to show reduced GPR when using the optimized ARLFO value, likely due to the inherent heterogeneity of thoracic anatomy. To validate this hypothesis, lung cases were excluded from the dataset used for the local gamma criterion analysis and Wilcoxon test was re-performed. The resulting p-value dropped to 0.0161, thus reaching statistical significance.

Looking ahead, future work will involve expanding the clinical dataset in order to elucidate the relationship between plan complexity and ARLFO sensitivity, ultimately enabling the identification of an optimal combination of MLC-related parameters for predicting the most appropriate ARLFO value. Moreover, the proposed methodology will be extended to additional beam energies, including 10X, 6FFF, and 10FFF.

In conclusion, the analytical approach presented in this thesis has demonstrated its feasibility and clinical relevance in enhancing PSQA through an optimal ARLFO parameter in Monte Carlo-based independent dose calculation. The results emphasize the importance of aligning model parameters with the realities of clinical practice, thus fostering the evolution of verification strategies that are more precise, adaptable, and tailored to individual patients.

Appendix A

Matlab Script

```
folderIN = 'RP_Plan';
folderE = {'Output_parameters'};

for en = 1:length(folderE)
    folderOUT = [folderIN, '/Output_parameters/', folderE{en}];
    pathE{en} = [folderIN, '/', folderE{en}];
    a = dir(pathE{en});
    at = struct2table(a);
    str2v = ['...working on folder ', num2str(folderE{en}), ...
            ', ', num2str(sum(at.isdir==0)), ' plan files to process ...'];
    disp(str2v);
    PList = at(at.isdir == 0, :);

    ID_List = cell(height(PList),1);
    RP_List = cell(height(PList),1);
    E_List  = cell(height(PList),1);

    for frtp = 1:height(PList)
        str2v = ['... working on file ', num2str(frtp), ':', PList.name{frtp}, ' ...'];
        disp(str2v);
        RP_File = [PList.folder{frtp}, '/', PList.name{frtp}];

        [ID, RP, E, medianGap, medianGap_nozeroes, perc_4] = ...
            MLC2Output_parameters(RP_File, folderOUT, PList.name{frtp});

```

```
26          ID_List{frtp} = ID;
27          RP_List{frtp} = RP;
28          E_List{frtp}  = E;
29          medianGap_List(frtp,1)            = medianGap;
30          medianGap_nozeroes_List(frtp,1)   = medianGap_nozeroes;
31          perc4_List(frtp,1)                = perc_4;
32      end
33  end
34
35  PList.ID = ID_List;
36  PList.RP = RP_List;
37  PList.E  = E_List;
38  PList.MLCGap_median           = medianGap_List;
39  PList.MLCGap_median_nozeroes  = medianGap_nozeroes_List;
40  PList.perc_min_4              = perc4_List;
41
42  writetable(PList, append(folderIN, '/Output_parameters/', '
        Output_file.xlsx'));
43
44  % Function definition
45  function [ID, RP, E, medianGap, medianGap_nozeroes, perc_4] =
        ...
46          MLC2Output_parameters(RP_File, folderOut, PList_name)
47
48  RP_info = dicominfo(RP_File);
49
50  w(1:14)   = 10;
51  w(15:46)  = 5;
52  w(47:60)  = 10;
53  lpos = cumsum(w) - 225;
54
55  fields = struct2cell(RP_info.BeamSequence);
56  nfields = length(fields);
57
58  ID = RP_info.PatientID;
59  RP = RP_info.RTPlanLabel;
60  E  = RP_info.BeamSequence.Item_1.ControlPointSequence.Item_1.
        NominalBeamEnergy;
61
62  allGaps = [];
63
64  for nf = 1:nfields
```

```
65      cp  = struct2cell(fields{nf}.ControlPointSequence);
66      ncp = length(cp);
67      for n = 2:ncp
68          if isfield(cp{n}.BeamLimitingDevicePositionSequence, '
                Item_3')
69              MLC1 = cp{n}.BeamLimitingDevicePositionSequence.
                    Item_3.LeafJawPositions;
70          else
71              MLC1 = cp{n}.BeamLimitingDevicePositionSequence.
                    Item_1.LeafJawPositions;
72          end
73          MLCA = MLC1(1:60);
74          MLCB = MLC1(61:120);
75
76          gap = MLCB - MLCA;
77          allGaps = [allGaps; gap(:)];
78      end
79  end
80
81  allGaps_nozeroes = nonzeros(allGaps);
82  medianGap          = median(allGaps);
83  medianGap_nozeroes = median(allGaps_nozeroes);
84
85  numero_cp_tot = numel(allGaps_nozeroes);
86  n_el_min_4    = sum(allGaps_nozeroes < 4);
87  perc_4        = n_el_min_4 / numero_cp_tot * 100;
88
89  end
```

References

[1] R. Baskar, K. A. Lee, R. Yeo, and K.-W. Yeoh, "Cancer and radiation therapy: current advances and future directions", International Journal of Medical Sciences **9**, Open-access article under Creative Commons license, 193–199 (2012).

[2] World Health Organization, *Cancer – fact sheet*, https://www.who.int/news-room/fact-sheets/detail/cancer, Accessed 30 June 2025, World Health Organization, 2022.

[3] D. Dance, S. Christofides, A. Maidment, I. McLean, and K. Ng, *Diagnostic radiology physics: a handbook for teachers and students* (International Atomic Energy Agency, 2014).

[4] T. Pawlicki, D. J. Scanderbeg, and G. Starkschall, *Hendee's radiation therapy physics*, 4th ed. (John Wiley & Sons, Hoboken, New Jersey, 2016).

[5] E. B. Podgoršak, *Radiation physics for medical physicists*, 3rd ed., Graduate Texts in Physics (Springer International Publishing, Cham, Switzerland, 2016).

[6] R. P. Symonds, C. Deehan, C. Meredith, and J. A. Mills, eds., *Walter & miller's textbook of radiotherapy: radiation physics, therapy and oncology*, 7th ed. (Churchill Livingstone / Elsevier, 2012).

[7] F. Cmreček, I. Andrašek, M. S. Mekić, M. Ravlić, and L. Beketić-Orešković, "Modern radiotherapy techniques", Libri Oncologici **47**, 91–97 (2019).

[8] L. M. Aggarwal, S. C. Sharma, and S. D. Sharma, *Intensity modulated radiation therapy: a clinical overview* (Jaypee Brothers Medical Publishers, 2015).

[9] M. Miften, A. Olch, D. Mihailidis, J. M. Moran, T. Pawlicki, A. Molineu, H. Li, K. Wijesooriya, J. Shi, P. Xia, N. Papanikolaou, and D. A. Low, "Tolerance limits and methodologies for imrt measurement-based verification qa: recommendations of aapm task group no. 218", Medical Physics **45**, e53–e83 (2018).

[10] *Prescribing, recording, and reporting intensity-modulated photon-beam therapy (imrt)*, tech. rep. Report 83 (International Commission on Radiation Units and Measurements, 2010).

[11]IAEA and AAPM, *Dosimetry of small static fields used in external beam radiotherapy: an iaea–aapm international code of practice*, Technical Reports Series No. 483 (International Atomic Energy Agency, Vienna, 2017).

[12]M. Karlsson, B. Mijnheer, H. Palmans, et al., *Implementation of psqa for treatment planning and dose delivery*, ESTRO Booklet No. 10 (European Society for Radiotherapy and Oncology (ESTRO), Brussels, Belgium, 2021).

[13]M. Miften, A. Olch, D. Mihailidis, J. Moran, T. Pawlicki, S. Stathakis, P. Xia, and T. C. Zhu, "Tqa task group 219: independent calculation-based dose/mu verification for imrt and vmat", Medical Physics **48**, e850–e871 (2021).

[14]P. Majewska, T. Janssen, K. Parodi, L. L. Andersen, H. Paganetti, M. Schwarz, W. Hälg, Ø. S. Bruland, P. L. D. Roover, E. Bezak, et al., *The use of independent dose calculation in the clinical practice*, tech. rep. (ESTRO (European Society for Radiotherapy and Oncology), 2021).

[15]A. Ahnesjö and M. M. Aspradakis, "Dose calculations for external photon beams in radiotherapy", Physics in Medicine and Biology **44**, R99–R155 (1999).

[16]F. De Martino, S. Clemente, C. Graeff, G. Palma, and L. Cella, "Dose calculation algorithms for external radiation therapy: an overview for practitioners", Applied Sciences **11**, 6806 (2021).

[17]E. Bezak, A. H. Beddoe, L. G. Marcu, M. Ebert, and R. Price, *Johns and cunningham's the physics of radiology*, 5th ed. (Charles C Thomas, Publisher, Ltd., Springfield, IL, 2021).

[18]G. Sceni, A. Botti, M. Orlandi, D. Lambertini, D. Finocchiaro, A. Barani, V. Bertolini, V. Trojani, R. Sghedoni, and M. Iori, "Tuning and validation of the new radcalc 3d monte carlo based pre-treatment plan verification tool", Journal of Mechanics in Medicine and Biology **23**, 2340047 (2023).

[19]Varian Medical Systems, Inc., *Eclipse photon and electron algorithms reference guide*, Document ID: P1008611-003-C, Eclipse version 13.6 (Palo Alto, CA, USA, Mar. 2015).

[20]S. Stathakis, P. Myers, C. Esquivel, P. Mavroidis, and N. Papanikolaou, "Characterization of a novel 2d array dosimeter for patient-specific quality assurance with volumetric arc therapy", Medical Physics **40**, 071710 (2013).

[21]D. A. Low, W. B. Harms, S. Mutic, and J. A. Purdy, "A technique for the quantitative evaluation of dose distributions", Medical Physics **25**, 656–661 (1998).

[22]N. Dogan, B. J. Mijnheer, K. Padgett, A. Nalichowski, C. Wu, M. J. Nyflot, A. J. Olch, N. Papanikolaou, J. Shi, S. M. Holmes, J. Moran, and P. B. Greer, "AAPM Task Group Report 307: Use of EPIDs for patient-specific IMRT and VMAT QA", Medical Physics **50**, e865–e903 (2023).

[23]E. Cagni, C. Mordacchini, S. Pittera, A. Bruschi, M. P. Petrillo, A. El Ouati, and S. Russo, "3242 application of estro commissioning protocol to a commercial solution for secondary check and epid-based in vivo dosimetry: a multicenter study", Radiotherapy and Oncology **206**, Abstract presented at ESTRO 2025, published in journal supplement, S2624–S2625 (2025).

[24]M. Esposito, L. Marrazzo, E. Vanzi, S. Russo, S. Pallotta, and C. Talamonti, "A validation method for epid in vivo dosimetry algorithms", Applied Sciences **11**, 10.3390/app112210715 (2021).